Available online at www.sciencedirect.com

ScienceDirect

Geochimica et Cosmochimica Acta 278 (2020) 157–176

Geochimica et Cosmochimica Acta

www.elsevier.com/locate/gca

An experimental study of peridotite dissolution in eclogite-derived melts: Implications for styles of melt-rock interaction in lithospheric mantle beneath the North China Craton

Chunguang Wang[a,b,*], Mauro Lo Cascio[b,1], Yan Liang[b], Wenliang Xu[a]

[a] *College of Earth Sciences, Jilin University, Changchun 130061, China*
[b] *Department of Earth, Environmental and Planetary Sciences, Brown University, Providence, RI 02912, USA*

Received 29 March 2019; accepted in revised form 10 September 2019; available online 18 September 2019

Abstract

Interaction between eclogite-derived melt and peridotite has played an important role in modifying the cratonic lithospheric mantle and generation of high-Mg igneous rocks. To better understand the effect of peridotite physical state on melt-peridotite interaction, we conducted reaction experiments of lherzolite with two basaltic andesites and a ferro-basalt at temperatures of 1300 °C, 1375 °C, and 1425 °C and a pressure of 2 GPa using the reaction couple method. At 1300 °C, when lherzolite is subsolidus, its dissolution rate is slow, and it is mineralogically and texturally unchanged. Garnet and clinopyroxene precipitate at the melt-rock interface. The low-temperature reaction enriches the melt with SiO_2 and Na_2O, and depletes the melt with Al_2O_3, FeO, and CaO. At 1375 °C and 1425 °C, when the lherzolite is partially molten, the dissolution and re-equilibration rates are fast due to grain-scale process that involves dissolution, precipitation, and reprecipitation. Dissolution of olivine and precipitation of orthopyroxene produce a melt-bearing orthopyroxene-rich lithology at the melt-rock interface followed by a melt-bearing harzburgite and a melt-bearing lherzolite. The lithology near the interface can be an orthopyroxene-rich harzburgite or an orthopyroxenite depending on the reacting melt composition. The high-temperature reaction produces melt with increased MgO, FeO, CaO, and Mg#, and decreased SiO_2, Al_2O_3, and Na_2O. The dissolution rate obtained from the experiments is used to assess the survival of mantle xenoliths in the early Cretaceous high-Mg diorites. Combined with field observations from mantle samples, the experimental results provide insight into the style of eclogite-derived melt and peridotite interaction in the lithospheric mantle beneath the North China Craton. At the lithosphere-asthenosphere boundary, the reaction is dominated by the high-temperature regime, which produces orthopyroxene-rich lithologies such as orthopyroxene-rich harzburgite and orthopyroxenite-veined peridotite. Above the lithosphere-asthenosphere boundary where peridotite is subsolidus, the reaction is characterized by the low-temperature regime, which produces garnet-bearing or garnet-rich lithologies such as garnet pyroxenite, garnetite, and high-Mg granulite. Interactions between eclogite-derived melts and peridotite in the two regimes are responsible for the geochemical features of the early Cretaceous high-Mg igneous rocks from the North China Craton.

Keywords: Melt-peridotite reaction; Dissolution experiment; Eclogite partial melt; Lithospheric mantle; Harzburgite; Garnet pyroxenite; North China Craton; High-Mg igneous rock

---

* Corresponding author at: College of Earth Sciences, Jilin University, Changchun 130061, China.
E-mail address: c_wang@jlu.edu.cn (C. Wang).

[1] Now at ExxonMobil Upstream Research Company, 22777 Springwoods Village Parkway, Spring, TX 77389, USA.

https://doi.org/10.1016/j.gca.2019.09.022
0016-7037/

1. INTRODUCTION

Cratons are relatively stable tectonic units with ancient continental lithosphere. However, cratons may have experienced destruction, during which the lower part of a craton was detached from the upper part. Some examples include the North China Craton (e.g., Menzies et al., 1993, 2007; Gao et al., 2002; Zhang et al., 2002; Santosh, 2010), the southwestern part of the Kaapvaal Craton (Kobussen et al., 2008), the Wyoming Craton (Carlson et al., 1999), and the Brazil Craton (Beck and Zandt, 2002). Destruction of the North China Craton (NCC) has been a subject of extensive geological investigations. The NCC is composed of three tectonic divisions: the Eastern Block and Western Block have Archean basements, and the Trans-North China Orogen (TNCO) was formed by collision of the two blocks in the Paleoproterozoic (e.g., Zhao et al., 2000, 2001). It has been suggested that the root of the Eastern Block was destabilized and experienced thinning during Mesozoic (e.g., Zhu et al., 2012). Proposed destruction mechanisms include delamination of lower continental lithosphere (e.g., Gao et al., 2004, 2008), thermo-chemical erosion (e.g., Fan and Menzies, 1992; Menzies and Xu, 1998; Zhang et al., 2003, 2005; Xu et al., 2004), and extension of lithosphere caused by Pacific slab subduction (e.g., Niu, 2005; Wu et al., 2018). Among these mechanisms, delamination of continental lithosphere is believed to play an important role in generating mantle heterogeneity and compositional variation of the late Mesozoic igneous rocks in the Eastern Block and TNCO. Eclogite formed by high to ultrahigh pressure metamorphism of basaltic lower continental crust can founder into the convecting mantle (e.g., Rudnick and Fountain, 1995; Anderson, 2006). Melt derived from the foundered eclogite reacts with overlying mantle peridotite forming high-Mg igneous rocks and a variety of lithologies in the mantle (e.g., Gao et al., 2004, 2008; Xu et al., 2008, 2010).

Early Cretaceous diorites from the Eastern Block and TNCO of NCC entrain spinel peridotite xenoliths with varying lithologies (e.g., Chen and Zhou, 2005; Xu et al., 2008, 2010; Wang et al., 2018). Some of harzburgite and dunite xenoliths have orthopyroxenite veins, which often contain hydrous minerals (amphibole and phlogopite) and have an interesting texture with orthopyroxene enclosing resorbed olivine grains. These peridotites are suggested to be products of reaction between the ancient cratonic lithospheric mantle and melts derived from delaminated lower crust (Xu et al., 2008, 2010; Wang et al., 2018). Zheng et al. (2007) reported spinel harzburgite xenoliths entrained by the Late Cretaceous basalts from Fuxin on the northern margin of the Eastern Block. The harzburgites are orthopyroxene-rich (31–34% in modal abundance), clinopyroxene-free, without hydrous mineral, and have olivines with a high Mg# [92, Mg# = 100 × Mg/(Mg + Fe), atomic ratio]. Harzburgite xenoliths with similar petrologic features are also found in the Cenozoic basalts from Hebi in the TNCO (26% orthopyroxene on average, 92–93 olivine Mg#, Zheng et al., 2001; Tang et al., 2013). These harzburgites are interpreted to be relics of the Archean cratonic mantle. However, such high modal abundance of orthopyroxene is unlikely resulted from partial melting of peridotite in the upper mantle (Kelemen et al., 1998). Liu et al. (2005) described a suite of spinel lherzolite, garnet pyroxenite, and granulite xenoliths from Hannuoba on the northern end of the TNCO. The garnet pyroxenites occur as veins in the host lherzolites, and there is a gradual decrease in olivine modal abundance and an increase in orthopyroxene modal abundance from the lherzolite to the pyroxenite. The garnet pyroxenites and intermediate to mafic granulites are both high in Ni and Mg#. Liu et al. (2005) attributed these petrologic and geochemical features to interaction between lherzolite and siliceous melt derived from recycled continental crust.

Based on laboratory partial melting experiments, melts derived from recycled crustal materials (pyroxenite or eclogite) are generally low in MgO and high in SiO_2 ($MgO < 8$ wt%, $SiO_2 > 47$ wt%), although low-silica melts can also be produced by melting silica-deficient pyroxenites in volatile-bearing systems (Fig. S1 in the Electronic Annexes). Reaction between pyroxenite or eclogite-derived melt and mantle peridotite was examined in a number of experimental studies. In particular, results of Yaxley and Green (1998) and Rapp et al. (1999) have been frequently used to interpret the melt-rock reaction features observed in igneous rocks and mantle xenoliths from the NCC (e.g., Gao et al., 2004, 2008; Chen and Zhou, 2005; Liu et al., 2005; Xu et al., 2008). These experiments were run at high pressures (3.5 and 3.8 GPa) using materials for starting melt with similar compositions. When the starting melt-to-rock ratio is low, melt was consumed by the reaction. When the starting melt-to-rock ratio is high, the reaction product depends on run temperature. Reactions at a relatively low temperature (1100 °C) resulted in high-Mg dacitic melts and a garnet-rich reaction zone (garnet ± orthopyroxene, Rapp et al., 1999). Reactions at relatively high temperatures (1250–1425 °C) produced high-Mg picritic melts and an orthopyroxene-rich reaction zone (orthopyroxene + olivine + clinopyroxene + garnet), and as temperature increases (to 1500–1550 °C), clinopyroxene and garnet vanished from the reaction front (Yaxley and Green, 1998).

Morgan and Liang (2005) and Wang et al. (2013) examined the lithology and mineral compositional variations formed by reaction between lherzolite and a basaltic andesite or a ferro-basalt at 1300–1425 °C and 1–2 GPa. They showed that the lithology produced by melt-rock reaction is controlled by the liquidus phase relationship of the reacting melt. At the run conditions, the silica-saturated basaltic andesite and ferro-basalt preferentially dissolve olivine and precipitate orthopyroxene resulting in a thin melt-bearing orthopyroxenite (<70 μm thick) and a melt-bearing harzburgite at the reaction front. Wang et al. (2013) compared mineral compositional variations obtained from the melt-rock experiments with those from the field observations of NCC mantle xenoliths. They suggested that lithospheric mantle beneath the NCC experienced interactions with pyroxenite or eclogite-derived melts in the Early Cretaceous, and that the interaction took place in the ancient orogens, such as the TNCO and the west of the Sulu Orogen in the Eastern Block. Wang et al. (2016) conducted experiments that reacted hydrous basaltic andesite or ferrobasalt with peridotites. These experiments produced a high-porosity orthopyroxenite reactive boundary layer (up to 770 μm thick in 3 h reaction). The orthopyroxenite-peridotite assembly and texture of the reaction product are nearly identical to those observed in mantle xenoliths entrained by the Early Cretaceous diorites from the Eastern Block and TNCO of the NCC.

Although considerable progress has been made to understand the mechanisms and consequences of melt-rock reaction that modified lithospheric mantle and the formation of igneous rocks from the NCC, a number of important issues regarding peridotite and eclogite-derived melt interaction remain unanswered. For example, how does the physical state of the peridotite (i.e., subsolidus or partially molten) affect the rate and mechanism of melt-rock reaction? How will such reaction affect melt composition? At what condition can a mantle xenolith survive its transport in an eclogite-derived melt? In this study, we report results of experiments of lherzolite dissolution in eclogite-derived melts at 2 GPa using the dissolution couple method. The experiments are conducted at 1300 °C when the lherzolite is subsolidus and 1375 °C and 1425 °C when the lherzolite is partially molten. Three eclogite-derived melts are considered: two basaltic andesites and a ferrobasalt. Based on the experimental results, we explore the style of reactions between the ancient NCC lithospheric mantle with melt derived from the recycling crustal materials, and the genesis of the geochemical features of late Mesozoic high-Mg basalts and diorites from the NCC. In the next section, we briefly describe the starting materials and experimental methods. We then present our experimental results focusing on dissolution rates, lithology, and phase compositions. Finally, we discuss the effect of lherzolite physical state on the rate, style, and melt compositional variations of melt-rock reaction, and apply the experimental findings on the field observations from the NCC. We show that peridotite physical state is an important factor in controlling the rate and style of melt-rock reaction, and that different reaction regimes are active in different parts of the lithospheric mantle, which has important implications for the modification of the lithospheric mantle and generation of compositional variation of high-Mg magmas in the NCC.

2. EXPERIMENTAL AND ANALYTICAL METHODS

Experiments characterizing lherzolite dissolution in eclogite-derived melts were carried out at 2 GPa in a 19.1 mm piston-cylinder apparatus at Brown University using the dissolution couple method. The run temperatures were 1300 °C, 1375 °C, and 1425 °C. At the run conditions, the three starting basalts are completely molten. The lherzolites are subsolidus at 1300 °C but partially molten at 1375 °C and 1425 °C.

2.1. Starting compositions

Three starting melts (Mont147, JG1-26 and JG4-1) and peridotites (KBH-1, WFY-1, and WFY-2) were used in the present study. Compositions of these starting materials are listed in Table 1. Major element compositions of the starting melts are within the composition range defined by eclogite and garnet pyroxenite partial melting experiments (Supplementary Fig. S1). Sample Mont147 is a basaltic andesite (55 wt% SiO_2, Mg# 45) from Montserrat. Samples JG1-26 and JG4-1 are a gneiss xenolith and an amphibole-bearing garnet clinopyroxenite xenolith from Xu-Huai, China (Xu et al., 2009). Their bulk compositions correspond to basaltic andesite (53 wt% SiO_2, Mg# 47) and ferro-basalt (47 wt% SiO_2, Mg# 45), respectively. Peridotite KBH-1 (49.0 wt% olivine, 35.5 wt% orthopyroxene, and 15.5 wt% clinopyroxene) was made from optically clean handpicked minerals from a fertile spinel lherzolite xenolith from Kilbourne Hole, New Mexico, USA. WFY-1 is a fertile spinel lherzolite xenolith (52 wt% olivine, 33 wt% orthopyroxene, 13 wt% clinopyroxene, and 2 wt% spinel) from Huinan, China. WFY-2 (60 wt% olivine, 23 wt% orthopyroxene, 12 wt% clinopyroxene, and 5 wt% spinel) was obtained by mixing the optically clean handpicked mineral separates of WFY-1. The starting materials were ground separately in ethanol using an agate mortar and pestle for 2 h to obtain fine powders with grain sizes of 25–40 μm. The powders were placed in a 200 °C vacuum oven for at least 12 h to drive off adsorbed water and stored at 110 °C before use.

2.2. Experimental procedures

Three sets of reaction couples were experimented in this study: one used in the Pyx experiments (Mont147 versus lherzolite, Fig. 1a) is similar to that in Morgan and Liang (2005), and the other two used in the 26W experiments (JG1-26 versus lherzolite, Fig. 1b) and the JW experiments (JG4-1 versus lherzolite, Fig. 1c) are identical to those in Wang et al. (2013). The Pyx experiments were run at 1300 °C and 1375 °C to test the effect of peridotite physical state and temperature on melt-rock reaction (Lo Cascio, 2008). The 26W and JW experiments were conducted to examine the variations of lithological sequence and dissolution rate with melt and lherzolite compositions (i.e., degree of undersaturation, see Section 4.2). Given the more primitive compositions of JG1-26 (53.5 wt% SiO_2 and 16.7 wt% Al_2O_3) and JG4-1 (47.5 wt% SiO_2 and 11.8 wt% Al_2O_3) than MONT147 (55.1 wt% SiO_2 and 19.0 wt% Al_2O_3), the 26W and JW experiments were run at a higher temperature (1425 °C).

The reaction couples were made by juxtaposing a pre-synthesized melt rod (top) against a pre-synthesized lherzolite rod (bottom). The melts and lherzolites were synthesized in graphite-lined molybdenum capsules at the same temperatures and pressures as the actual dissolution runs for 2.75–12 h and 48 h, respectively, to produce mineral-free glass rods with homogeneous compositions and lherzolite rods with homogeneous textures. This procedure prevents spontaneous melt infiltration during melt-rock reaction compared with the powder-to-powder reaction couple setup. It also minimizes the impact of using natural starting materials on dissolution rate and reaction result compared with using sintered starting materials.

Table 1
Starting compositions.

Sample	SiO_2	TiO_2	Al_2O_3	Cr_2O_3	FeO	MnO	MgO	CaO	Na_2O	K_2O	NiO	P_2O_5	Mg#
Eclogite-derived melts													
Mont147[a]	55.08	0.79	19.03	–	8.42	0.22	3.86	8.80	2.97	0.71	–	0.13	44.97
JG1-26[b]	53.45	1.39	16.68	–	11.37	0.17	5.81	8.29	2.36	0.32	–	0.16	47.69
JG4-1[b]	47.46	1.72	11.75	–	18.23	0.26	8.33	11.70	0.47	0.04	–	0.04	44.89
Lherzolites													
KBH-1[a]	46.92	0.09	3.05	0.37	6.99	0.13	38.81	3.27	0.23	–	0.15	–	90.82
WFY-1[b]	45.94	0.09	3.31	0.51	7.83	0.12	38.73	3.04	0.17	–	0.25	–	89.81
WFY-2[b]	43.19	0.08	4.45	0.85	8.30	0.12	39.82	2.75	0.15	–	0.28	–	89.54

Oxide concentrations are in wt%. Bulk compositions of the starting lherzolites are calculated using compositions and modal abundances of the constituent minerals. The starting compositions are normalized to total 100 wt%. Mg# is defined as atomic ratio 100 × Mg/(Mg + Fe). Total Fe as FeO.

[a] Mont147 and KBH-1 is from Morgan and Liang (2005).

[b] JG4-1, JG1-26, WFY-1, and WFY-2 are from Wang et al. (2013).

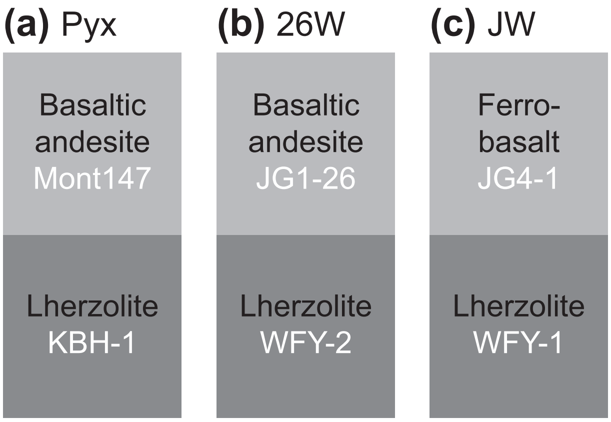

Fig. 1. Schematic diagram illustrating the three types of dissolution couple used in this study.

After each pre-synthesis run, the molybdenum-graphite capsule was cut in half perpendicular to the cylindrical axis using a low-speed diamond saw. The exposed surface was polished to 23 μm and cleaned in ethanol in a sonicator. Thin platinum strips were placed longitudinally around the reaction couple. Platinum alloys with molybdenum at the run conditions, which helps prevent the two rods from separating during quench. A small offset is formed between the two rods when assembling a reaction couple, which serves as a marker for the original melt-rock interface.

Furnace assembly and run procedures are identical to those described in Wang et al. (2013). Experimental conditions are listed in Table 2. The retrieved reaction couple was cut longitudinally, mounted in epoxy, and polished to expose the cylindrical center of the experimental charge, and then polished to 1 μm finish for electron microprobe analysis.

2.3. Microprobe analysis

Back-scattered electron (BSE) images, X-ray concentration maps, glass, and mineral chemical analyses were conducted using a Cameca SX-100 electron microprobe at Brown University. An accelerating voltage of 20 kV and a beam current of 50 nA were used to collect BSE images and X-ray concentration maps. Glasses with quench crystals and quench-free glasses were analyzed using a 10-μm-diameter defocused beam and a 5-μm-diameter defocused beam, respectively, with an accelerating voltage of 15 kV and a current of 10 nA. Minerals were analyzed using a focused beam with an accelerating voltage of 20 kV and a current of 25 nA. Counting times were 20 s for peak and 10 s for background on each side of the peak. To minimize sodium loss during the analyses, sodium was analyzed first. Natural standards were used for calibration. For small mineral grains exposed on the polished surface of samples, we tried to analyze their central parts. Even so, the analyses (such as Ca in olivine and Na in orthopyroxene) could potentially be affected by secondary fluorescence effects, but this is of no consequence to the conclusions reached in this study.

2.4. Distance measurements

Dissolution distance and thickness of reactive boundary layers were measured using the BSE images. Dissolution distance is the distance between the current interface and the original interface which is marked by the offset. All the measurements were conducted around the central part of each experimental charge for at least 5 times. In some experimental charges, cracks were formed around the interface region during quench. Widths of the cracks were measured and subtracted from the distances before taking average. The average dissolution distance and thicknesses of reactive boundary layers of each run are listed in Table 2.

3. RESULTS

All the reaction experiments reported in this study were conducted at 2 GPa. Figs. 2 and 3 display the BSE images for the charges of representative experiments. Fig. 4 plots the measured dissolution distance and thicknesses of reactive boundary layers as a function of the square root of run duration. Figs. 5–7 show the variations of melt, olivine,

Table 2
Summary of lherzolite dissolution experiments.

Run#	Duration (h)	Initial glass length (μm)	Initial lherzolite length (μm)	Dissolution distance[c] (μm)	Opx-rich layers thickness[c] (μm)	Orthopyroxenite thickness[c] (μm)
Low-T, 1300 °C; Basaltic andesite (Mont147)[a]						
Pyx3	6	1627	1764	26 ± 9	–	–
Pyx10	24	1094	2095	34 ± 2	–	–
Pyx11	74	1187	827	34 ± 25	–	–
High-T, 1375 °C; Basaltic andesite (Mont147)[a]						
Pyx26	0.5	776	1845	29 ± 2	0	–
Pyx21	2	1280	1440	110 ± 38	102 ± 32	–
Pyx27	24	2230	2068	348 ± 21	702 ± 194	–
Pyx16	24	930	164	173 ± 13	–	–
Pyx17	24	721	2094	160 ± 23	–	–
Pyx20	74	1760	1112	394 ± 12	–	–
High-T, 1425 °C; Basaltic andesite (JG1-26)						
26W01	3	1644	1848	162 ± 12	883 ± 18	37 ± 17
26W02[b]	8	2931	2767	251 ± 32	1780 ± 39	53 ± 24
High-T, 1425 °C; Ferro-basalt (JG4-1)						
JW03[b]	3	2267	3267	218 ± 9	324 ± 46	69 ± 13
JW02	6	1935	1891	334 ± 25	739 ± 16	98 ± 9

[a] Experiments from Lo Cascio (2008).
[b] Experiments from Wang et al. (2013).
[c] One standard deviation estimated from at least 5 measurements around the central portion of a given charge.

and pyroxene compositions. Additional BSE images, garnet composition profiles, and the electron microprobe data can be found in the Electronic Annexes (Figs. S2 and S3, Tables S1–12).

3.1. Experimental charge and textures

Fig. 2(a and b) displays regions near the melt-rock interface of two representative basaltic andesite and lherzolite reaction experiments at 1300 °C. At this run temperature, the lherzolite is subsolidus, and is mineralogically and texturally uniform in the charge. It is separated from the reacting melt by a narrow clinopyroxene transition layer of one mineral grain width. A few garnet grains are observed on the melt side of the interface, with clinopyroxenes included in some of the garnet grains (inset in Fig. 2b). The size (up to 150 μm in diameter) and number of garnet grains increase considerably over time (cf. Fig. 2a and Fig. 2b). Olivine and orthopyroxene are euhedral throughout the lherzolite with a median grain size of 40 μm and 30 μm, respectively. Clinopyroxene crystals are typically anhedral with a median grain size of 40 μm except those at the melt-lherzolite interface, where the grain size is very small (<10 μm). In these relatively low temperature experiments, dissolution distance is small and varies very little with time (Table 2).

Fig. 2(c and d) shows BSE images of representative reaction experiments conducted at high temperatures (1375 °C and 1425 °C). In these experiments, the lherzolites are partially molten with melt fractions of ~5 vol% at 1375 °C and ~7 vol% at 1425 °C. The lithological sequence and texture are significantly different from those in the 1300 °C experiments. The lherzolite reacts with the melt, resulting in distinct lithological regions. In general, the sequence of lithology from the melt-rock interface to the end of peridotite rod includes (1) an orthopyroxene-rich layer, (2) a harzburgite, and (3) a lherzolite, all of which are melt-bearing. Lithologies (1) and (2) are clinopyroxene-free. Lithology (1) is an orthopyroxene-rich harzburgite with an orthopyroxene-to-olivine ratio of ~1.5 in the 1375 °C Pyx experiments (Fig. 2c), and a pure orthopyroxenite (37–98 μm thick, Fig. 2d, Fig. S2, Table 2) in the 1425 °C experiments (26W and JW). Lithology (2) is also orthopyroxene enriched with orthopyroxene-to-olivine ratios of 0.5–1. In the longest duration run Pyx20 (74 h, 1375 °C), the peridotite half of the experimental charge is clinopyroxene-free, with the orthopyroxene-rich harzburgite surrounding the central harzburgite (Fig. 3). In general, melt proportion increases from Lithology (3) to Lithology (2) (Fig. 2c). Due to orthopyroxene crystallization, melt proportion decreases from Lithology (2) to Lithology (1) (Fig. 2(c, d) and Fig. S2), especially in the long duration run Pyx20 (Fig. 3). Olivine and orthopyroxene in Lithology (2) are euhedral to subhedral with median grain size of 50 μm and 45 μm, respectively. Orthopyroxene grains in Lithology (1) are larger than those in Lithology (2), and contain olivine inclusions, suggesting that growth of these orthopyroxenes are at the expense of olivine (insets in Fig. 2(c, d) and 3). Clinopyroxene crystals are typically anhedral with a median grain size of 25 μm. Garnet is not observed in the 1375 °C and 1425 °C experiments. Melts from the 1375 °C experiments are not affected by quench growth, except at the melt-rock interface region where we observe a zone (<40 μm) of dendritic quenched crystals. Dendritic quenched crystals grow 300 μm from the melt-rock interface in the 26W experiments, and they grow throughout the melt half in the JW experiments. A substantial amount of lherzolite is dissolved in the melts, and dissolution distance increases significantly with time (Table 2).

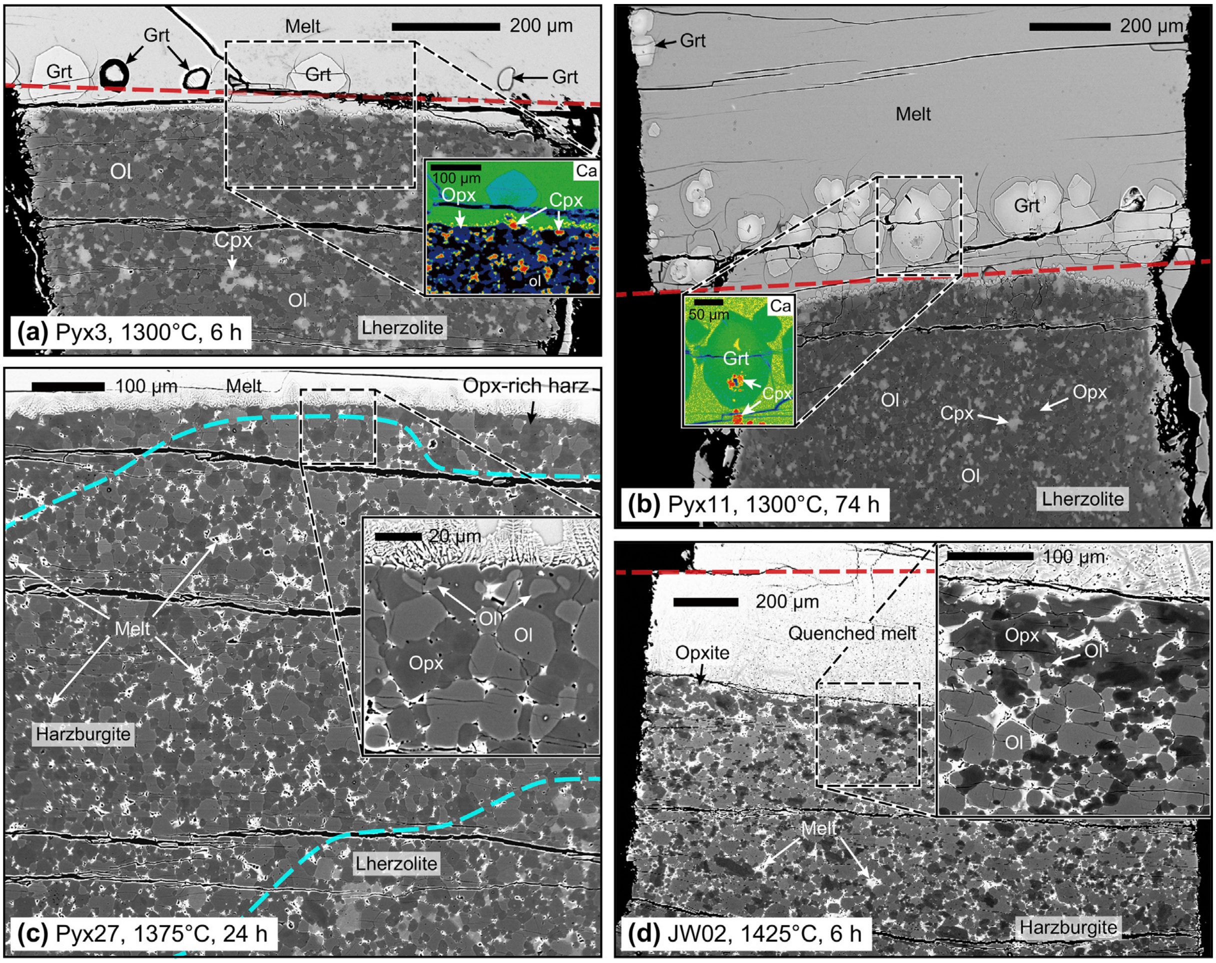

Fig. 2. Back-scattered electron (BSE) images of the representative experimental charges. All experiments were conducted at 2 GPa. Run temperature and duration are labeled in each panel. In the low-temperature dissolution experiments involving the basaltic andesite Mont147 (**a** and **b**), lherzolite is mineralogically and texturally unchanged with a small amount of dissolution; garnet grains and small clinopyroxene crystals are precipitated at the melt-rock interface (**a** and **b**). In the long duration low-temperature experiment (**b**), more garnet grains are precipitated. In the high-temperature dissolution experiment involving the basaltic andesite Mont147 (**c**), an orthopyroxene-rich harzburgite – harzburgite – lherzolite sequence is formed. In the high-temperature dissolution experiments involving the ferro-basalt JG4-1 (**d**), a melt-bearing orthopyroxenite layer is formed at the melt-rock interface, and the lherzolite near the melt-rock interface has been converted to melt-bearing harzburgite with a large amount of dissolution. The dashed red lines in **a**, **b**, and **d** mark the initial locations of the melt-rock interface, and the dashed cyan lines in **c** mark the boundaries of the orthopyroxene-rich harzburgite – harzburgite – lherzolite sequence. Insets in **a** and **b** are X-ray Ca concentration maps showing the mineralogy at the melt-rock interface. Ol: olivine, Opx: orthopyroxene, Cpx: clinopyroxene, Grt: garnet, Harz: harzburgite, Opxite: orthopyroxenite. (For interpretation of the references to colour in this figure legend, the reader is referred to the web version of this article.)

The widths of the newly formed harzburgite layers also increase, such that the lherzolite width decreases with time (Table 2).

3.2. Dissolution distance of peridotite and thickness of orthopyroxene-rich layers

At run conditions, the lherzolites are not in equilibrium with the starting melts, and hence they dissolve into the melts. The amount of dissolution can be quantified by dissolution distance. Fig. 4a plots the measured dissolution distances as a function of the square root of run time. For the relatively short-duration experiments, dissolution distance changes linearly with the square root of time (lines in Fig. 4a). This correlation is consistent with the kinetics of diffusive dissolution in an effective semi-infinite melt reservoir (Zhang et al., 1989; Liang, 1999, 2000, 2003; Chen and Zhang, 2008, 2009). However, when diffusion distance for major element in the melt is comparable to the initial length of the melt reservoir, composition of the far-field melt is affected by lherzolite dissolution, resulting in a reduction in driving force for dissolution. The initial glass rod used in experiments Pyx11, Pyx16, Pyx17, and Pyx20 are short (827–2094 μm) for their long run durations (24–74 h) (Table 2). This results in the short dissolution distances in Pyx16 and Pyx17 compared to Pyx27 (2230 μm initial glass for 24 h reaction) and the deviations of Pyx11, Pyx16, Pyx17, and Pyx20 data from the linear

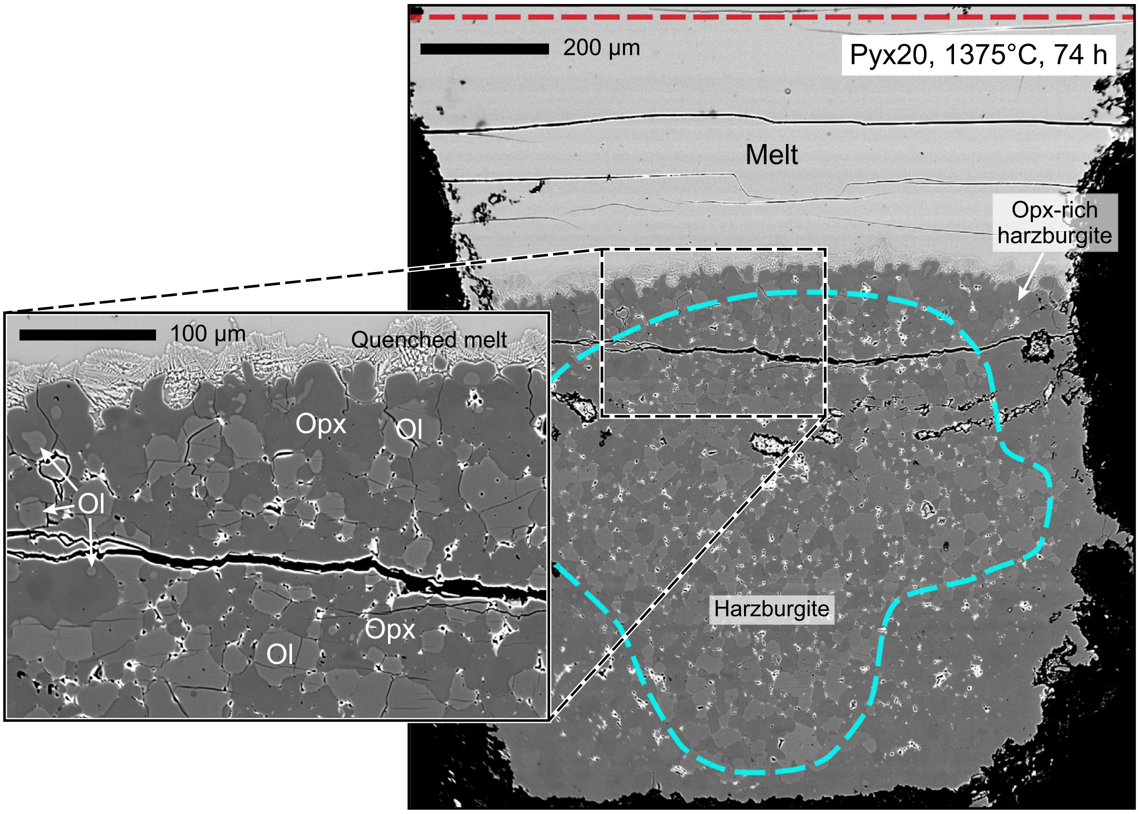

Fig. 3. Back-scattered electron (BSE) image of the central part of long-duration experiment Pyx20 (lherzolite versus Mont147, 1375 °C, 2 GPa, 74 h). The dashed red line marks the initial location of the melt-rock interface, and the dashed cyan curve delineates the boundary between the orthopyroxene-rich harzburgite and the central harzburgite. Ol: olivine, Opx: orthopyroxene. (For interpretation of the references to colour in this figure legend, the reader is referred to the web version of this article.)

relation in Fig. 4a. The finite melt geometry effect on diffusive dissolution is discussed in Liang (2003). Dissolution rate will be discussed in Section 4.2.

Fig. 4b displays the widths of orthopyroxene-rich layers as a function of the square root of the run duration for the experiments. Here the data are more scatter due to melt infiltration along the graphite-peridotite boundary in some of the experiments. Fig. 3 shows one example. In general, the orthopyroxene-rich layers from the 1425 °C experiments grow faster than the other experiments conducted at relatively low temperatures. The 1375 °C Pyx experiments have a lower harzburgite growth rate than the 1300 °C and 1 GPa ones from Morgan and Liang (2005) that have higher melt fractions (8–12%) in harzburgite than the formers (5%). The 26W experiments have a faster growth rate of the orthopyroxene-rich layers than the JW experiments, which is also in accordance with the variation of harzburgite melt fraction (15% versus 13%).

3.3. Melt and mineral compositions

Fig. 5 shows the melt compositions as a function of distance away from the final melt-rock interface normalized by square root of time. In general, from the far field to the melt-rock interface, the reacting melts become lower in TiO_2, Al_2O_3, CaO and Na_2O concentrations and higher in MgO and Mg#. The SiO_2 profiles in Pyx26 and JW03 and the FeO profiles in Pyx3, Pyx26 and JW03 show mild uphill diffusion patterns. In 26W02, SiO_2 and FeO concentrations in melt show monotonic variations. The experiments Pyx3 and Pyx26 that were run using the same reaction couple but at different temperatures (1300 °C versus 1375 °C) have different melt composition profiles (cyan and magenta circles in Fig. 5). First, SiO_2 concentration in the melt decreases towards the melt-rock interface in the high-temperature run whereas it increases in the low-temperature run. Second, towards the melt-rock interface, melt composition from the high-temperature run varies more significantly than that in the low-temperature run, such as the variations in TiO_2, FeO, MgO, CaO, Na_2O, and Mg#. And finally, near the melt-rock interface, Al_2O_3 concentration in melt from the low-temperature run decrease dramatically compared to the general decrease in the high-temperature run.

Fig. 6 displays the melt compositions in the pseudo-ternary system of forsterite – calcium-Tschermak – quartz projected from diopside using the method of O'Hara (1968). To the first order, the melt compositions in the high-temperature experiments are controlled by lherzolite dissolution, which vary towards the composition of lherzolites (red arrow in Fig. 6). Variation of the melt chemistry in the low-temperature experiments is primarily controlled by

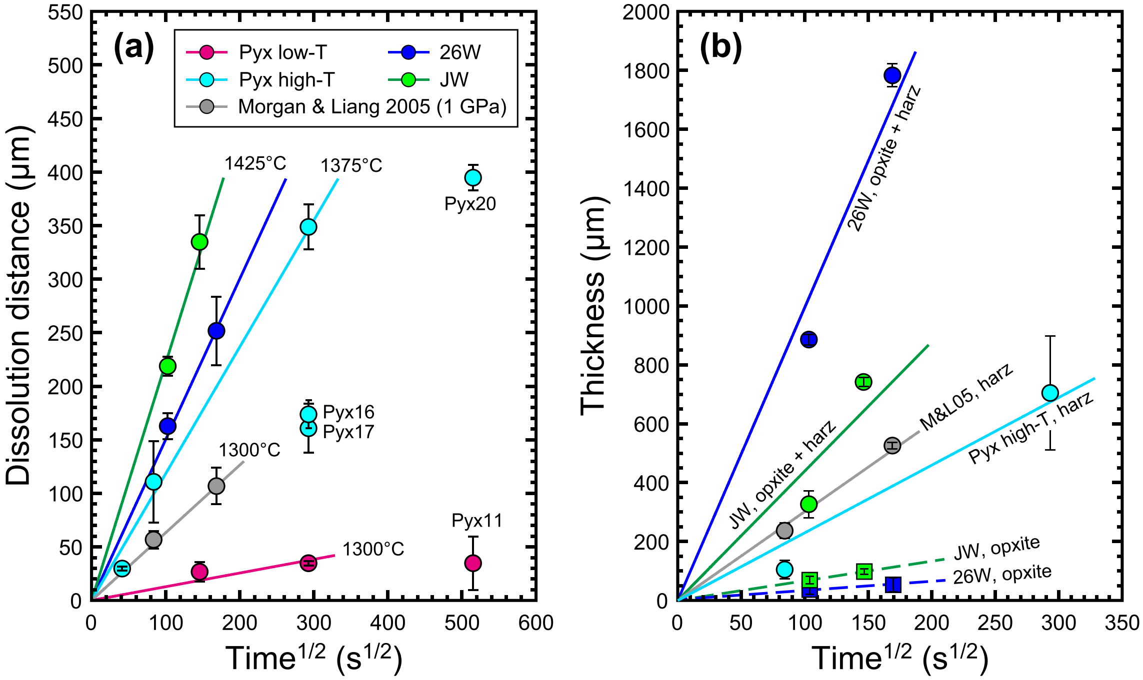

Fig. 4. Plots of dissolution distance (**a**) and thicknesses of orthopyroxene-rich layers (**b**) as a function of the square root of time for the melt-rock reaction experiments. The error bars represent 1 σ deviations below and above the mean values. The lines are best fit to the data. The experiments with shot melt rod with respect to run duration (Pyx16, Pyx17, Pyx20, and Pyx11) were not included in the fitting in **a**. Gray circles are data from experiments of basaltic andesite (Mont147) and lherzolite reaction at 1300 °C and 1 GPa in Morgan and Liang (2005). Opxite: orthopyroxenite, Harz: harzburgite.

garnet ± clinopyroxene crystallization and diffusive exchange between the starting basaltic andesite and the interface melt, which drives the melt compositions towards the quartz-enstatite join (blue arrows in the right panel of Fig. 6).

Olivine composition at 1300 °C is essentially constant and similar to the starting value (dashed blue lines in Fig. 7(a–c)) across the lherzolite, except at the melt-lherzolite interface in the long duration-experiment Pyx11 (74 h) where Mg# and Cr_2O_3 decrease, and CaO increases (Fig. 7(a–c)). By contrast, Mg# and Cr_2O_3 in olivine at 1375 °C decrease gradually with distance (Fig. 7(a and b)). CaO in olivine is constant and high compared to the 1300 °C experiments (Fig. 7c). Due to melting and re-equilibration during the synthesis, olivines at the far-field of the charge in the 1375 °C experiment have higher Mg#, Cr_2O_3, and CaO that those in the 1300 °C experiment.

In contrast to olivine, pyroxenes in the lherzolite regions have more scattered compositions (Fig. 7(d–h)). Compositions of pyroxenes from the 1300 °C experiment vary around the starting values (dashed green and red lines). Clinopyroxene crystallized on the melt side of the melt-lherzolite interface has low Mg# (79–88) and CaO (11.2–15.6 wt%), and high Al_2O_3 (6.4–10.4 wt%), distinct from that in the lherzolite. Orthopyroxene in lherzolite from the 1375 °C experiment has higher Mg# (up to 92), CaO, and Cr_2O_3, and lower TiO_2, Al_2O_3, NiO, and Na_2O than that from the 1300 °C experiment (Fig. 7(d–h), Tables S1 and S6). A trend of decreasing Mg# towards the interface is observed in orthopyroxene from the 1375 °C experiment (Fig. 7d). Clinopyroxene from the 1375 °C experiment has higher MnO, and lower CaO, TiO_2, Al_2O_3, NiO, and Na_2O than that from lherzolite in the 1300 °C run (Fig. 7 (e–h), Tables S1 and S6). Clinopyroxene is augite in the 1300 °C experiment and subcalcic augite in the 1375 °C experiment (Fig. 7i), consistent with the change of pyroxene solvus composition with temperature.

Garnets from the 1300 °C experiments develop core-to-rim compositional vitiations (Fig. S3). They grow rims with higher in Mg# and Cr_2O_3 content, whereas lower in CaO content than the cores. The rims have higher pyrope component and lower almandine and grossular components than the cores.

4. DISCUSSION

4.1. Grain-scale processes of eclogite-derived melt and lherzolite interaction

Systematic variations in melt and mineral compositions, lithology, and dissolution distances can be used to deduce the grain-scale processes governing eclogite-derived melt and peridotite interaction. The dissolution of lherzolite in eclogite-derived melts at 2 GPa takes place in two different regimes depending on whether the lherzolite is subsolidus or partially molten (Lo Cascio, 2008). At 1300 °C and 2 GPa, when the lherzolite is subsolidus, the processes involve simple dissolution of the lherzolite with crystallization of garnet ± clinopyroxene at the rock-melt interface.

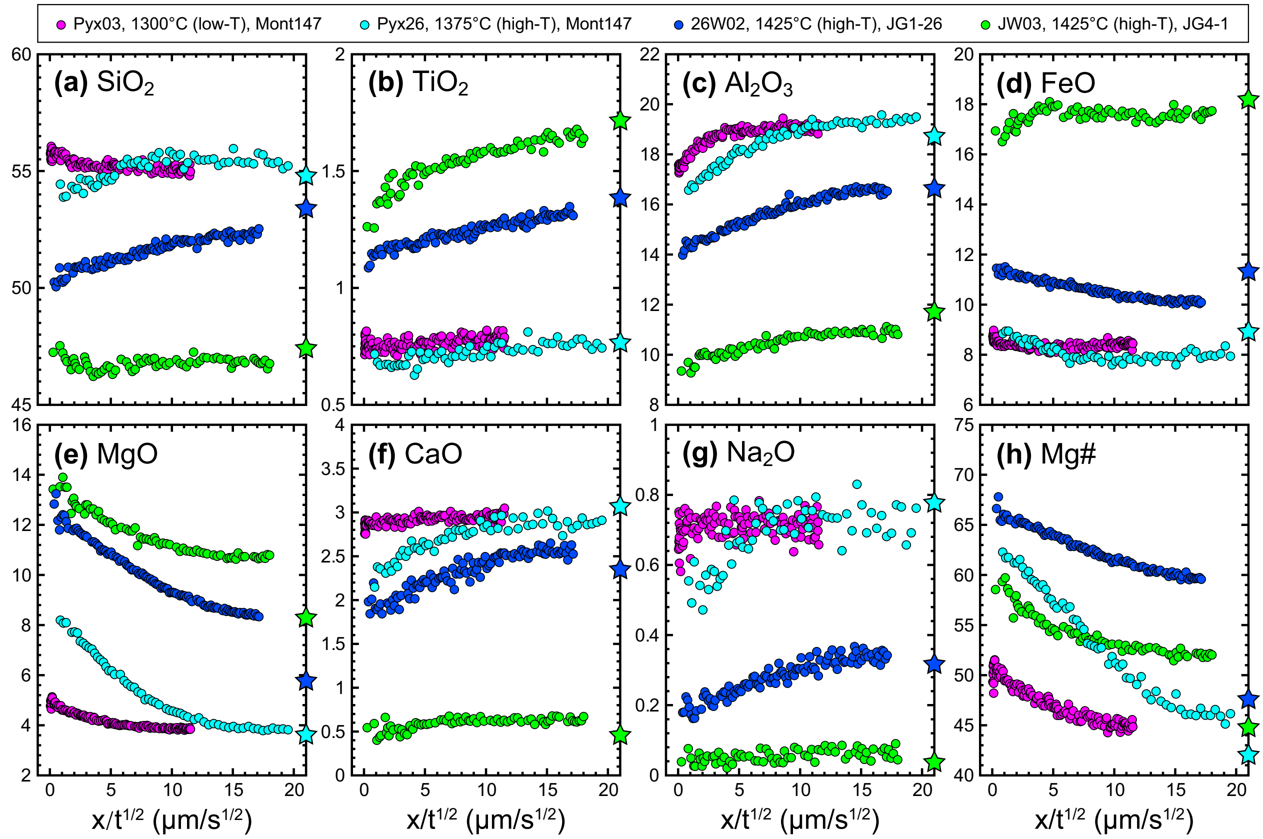

Fig. 5. Plots of oxide abundances (in wt%) and Mg# in melt as a function of distance away from the melt-rock interface (x) normalized by the square root of time (t) for representative dissolution experiments that have enough long melt rod with respect to run duration. Cyan, blue, and green pentagrams denote compositions of the starting melts Mont147, JG1-26, and JG4-1, respectively. (For interpretation of the references to colour in this figure legend, the reader is referred to the web version of this article.)

As described in 3.1 and 3.3, mineralogy, texture, and mineral compositions of the lherzolite are generally not affected by the reacting melt (Figs. 2(a, b) and 7). Even in the long-duration run (Pyx11, 74 h), olivine composition is altered within 50 μm from the interface (Fig. 7(a–c)). Clinopyroxenes precipitated at the melt side of the interface have different compositions from those in the lherzolite (Figs. 2(a, b) and 7(d, g–i)), which is a by-product of melt-lherzolite reaction at the interface. The increasing pyrope content from core to rim of garnet crystals in the reacting melt (Fig. S3) suggests a gradual dissolution of lherzolite in the melt during garnet growth (Fig. 2(a and b)). The variation of melt composition is in accordance with garnet ± clinopyroxene (cpx) crystallization (e.g., decrease in Al_2O_3 and increase in SiO_2) and diffusive exchange between the starting and interface melts (e.g., increase in MgO and Mg#, Fig. 5). Thus, the reaction between eclogite-derived melt and subsolidus lherzolite can be expressed as:

$$\text{lherzolite} + \text{melt}_1 \rightarrow \text{garnet} \pm \text{cpx} + \text{melt}_2, \quad (1)$$

where melt_1 is the starting melt; and melt_2 is the reacted melt at the melt-lherzolite interface where crystallizations of garnet and a small amount of clinopyroxene drive the melt composition towards the quartz-enstatite join (Fig. 6). Lithology of the reactive boundary layer depends on liquidus phase relationship of the reacting melt (Wang et al., 2013). Garnet and clinopyroxene are precipitated because they are on or near the liquidus of reacting melt at 2 GPa. It should be noted that liquidus phase relationship changes with pressure and melt composition. High pressures stabilize garnet on the liquidus, and high SiO_2 contents in MgO-rich systems (such as melt-peridotite) stabilize orthopyroxene relative to clinopyroxene on the liquidus. The reaction experiments of Rapp et al. (1999) were run at 1100 °C and 3.8 GPa, and partial melting of the starting eclogite at this condition produced a high-SiO_2 melt (66 wt%) for reaction. Thus, the reaction zone mainly comprised of garnet with orthopyroxene crystallized when the starting melt-to-peridotite ratio is low.

At 1375 °C and 1425 °C and 2 GPa, the lherzolite is partially molten. We observe significant mineralogical and textural changes in the peridotite (Fig. 2(c, d) and 3, Fig. S2) and the development of compositional gradients in the reaction couple (Figs. 5–7). The grain-scale processes are characterized by dissolution, precipitation, and reprecipitation of mineral phases (Liang, 2003; Morgan and Liang, 2003, 2005; Lo Cascio et al., 2004, 2008; Wang et al., 2013). The dissolution-reprecipitation processes not only change the distribution of minerals in the peridotite, but also speed up re-equilibration between peridotite and melt. Reaction between the partially molten lherzolite and the eclogite-derived melt can be written as

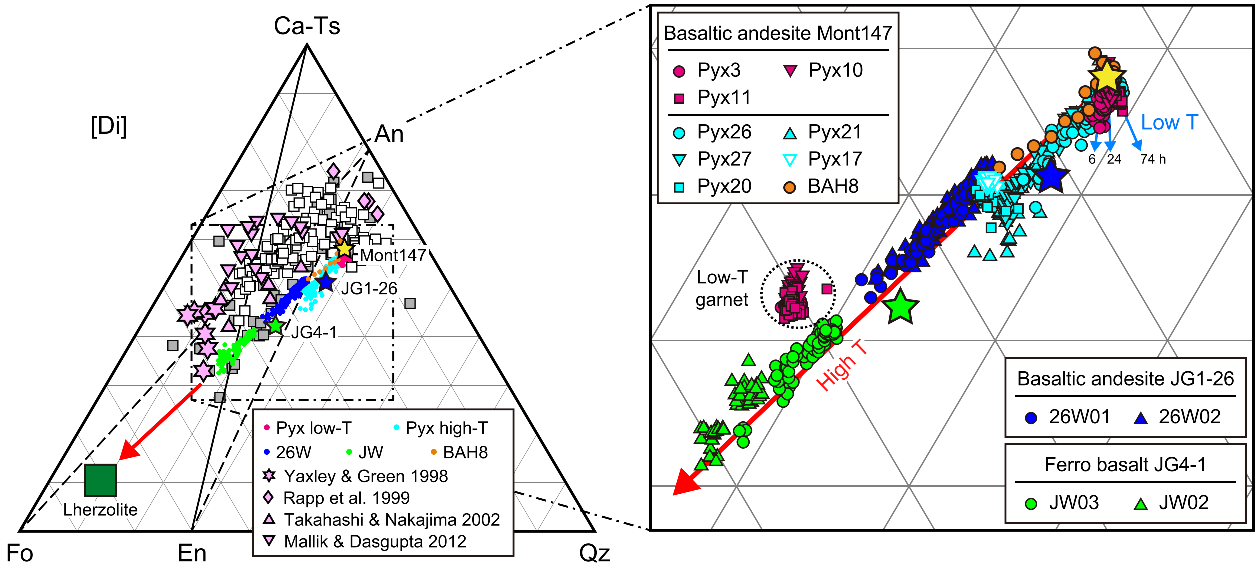

Fig. 6. Normative composition in the pseudo-ternary system of forsterite (Fo) – calcium Tschermak (Ca-Ts) – quartz (Qz) projected from diopside (Di) using the method of O'Hara (1968) for reacted melts from melt-rock reaction experiments. Orange circles are compositions of reacted melt from the hydrous melt and lherzolite reaction experiment (BAH8, 1 GPa and 1200 °C) from Wang et al. (2016) which used the same starting basaltic andesite (Mont147, 4 wt% water was added) as the Pyx experiments from this study. Light pink symbols are the compositions of reacted melts from previous melt-rock reaction studies (Yaxley and Green, 1998; Rapp et al., 1999; Takahashi and Nakajima, 2002; Mallik and Dasgupta, 2012). Data in the dashed circle are compositions of garnets at the melt side of the interface in the low-temperature runs. The red and blue arrows indicate melt compositional variation trends for the high-temperature (1375 °C and 1425 °C) and low-temperature (1300 °C) reaction experiments, respectively. The dark green square denotes composition range of the starting peridotites. The yellow, blue, and green pentagrams denote compositions of the starting melts Mont147, JG1-26, and JG4-1, respectively. Also plotted are field data from the NCC including late Mesozoic high-Mg igneous rocks (open squares, Zhang et al., 2002; Gao et al., 2004; Pei et al., 2004; Xu et al., 2006; Huang et al., 2008; Yang et al., 2006, 2008; Qian and Hermann, 2010; Xu et al., 2009; Wang et al., 2011; Chen et al., 2013) and high-Mg granulite xenoliths from Hannuoba (gray squares, Liu et al., 2001, 2005; Zhou et al., 2002). (For interpretation of the references to colour in this figure legend, the reader is referred to the web version of this article.)

$$(\mathrm{ol}_1 + \mathrm{opx}_1 + \mathrm{cpx}_1 + \mathrm{melt}_0) + \mathrm{melt}_1 \rightarrow \mathrm{ol}_2 + \mathrm{opx}_2 + \mathrm{melt}_2, \tag{2}$$

where melt_0 is partial melt of the starting lherzolite formed during synthesis; and subscripts 1 and 2 designate the melts and materials before and after the reaction. In contrast to the reaction at subsolidus state, part of the reacting melt_1 infiltrates (via diffusion through the interstitial melt_0) into the partially molten peridotite, dissolving minerals in the lherzolite and reprecipitating olivine (ol_2) and orthopyroxene (opx_2). Dissolution distance increases with time (Fig. 4a), indicating a substantial amount of lherzolite dissolution in the melt relative to the amount of reprecipitation. In the reactive boundary layer, the reprecipitation is characterized by a high orthopyroxene-to-olivine ratio because orthopyroxene is on the liquidus of melt_0 and melt_1 mixture. These grain-scale processes lead to the formations of orthopyroxenite and orthopyroxene-rich harzburgite and an interface melt (melt_2) with decreased SiO_2, Al_2O_3, and Na_2O and increased MgO and Mg# (Fig. 5).

4.2. Rates of peridotite dissolution and orthopyroxene-rich lithology growth

The rate of diffusive dissolution (V) depends on the degree of undersaturation (Θ) and is inversely proportional to the square root of time (Zhang et al., 1989; Liang, 1999):

$$V = \alpha\sqrt{\frac{D_f}{t}} \tag{3a}$$

$$\alpha \approx -0.7763\left(1 - \sqrt{1 + 1.4535\Theta}\right) \tag{3b}$$

$$\Theta = \frac{C_f^b - C_f^\infty}{C_s^b - C_f^b} \tag{3c}$$

where D_f is the diffusion coefficient of the rate limiting species; C_s^b is the solid composition at the melt-rock interface; C_f^b and C_f^∞ are the melt compositions at the interface and far-field, respectively. We use the effective binary diffusion coefficient (EBDC) to approximate D_f in multi-component melts (Cooper, 1968; Watson, 1982; Zhang et al., 1989). In a multi-component system, the melt and solid compositions at the interface changes with time (Liang, 2003), making Θ time-dependent. In practice, the variation of solid composition at the melt-rock interface (C_s^b) is relatively small compared to that of the melt composition. Thus, for simplicity, we assume that C_s^b is constant and equals to the bulk lherzolite composition. The concentrations profiles of melt in our experiments can be used to estimate C_f^b, C_f^∞, and thus Θ. According to the parabolic law of diffusive dissolution, dissolution distance (L) and dissolution rate (V) can be expressed as

$$L = k\sqrt{t} \tag{4a}$$

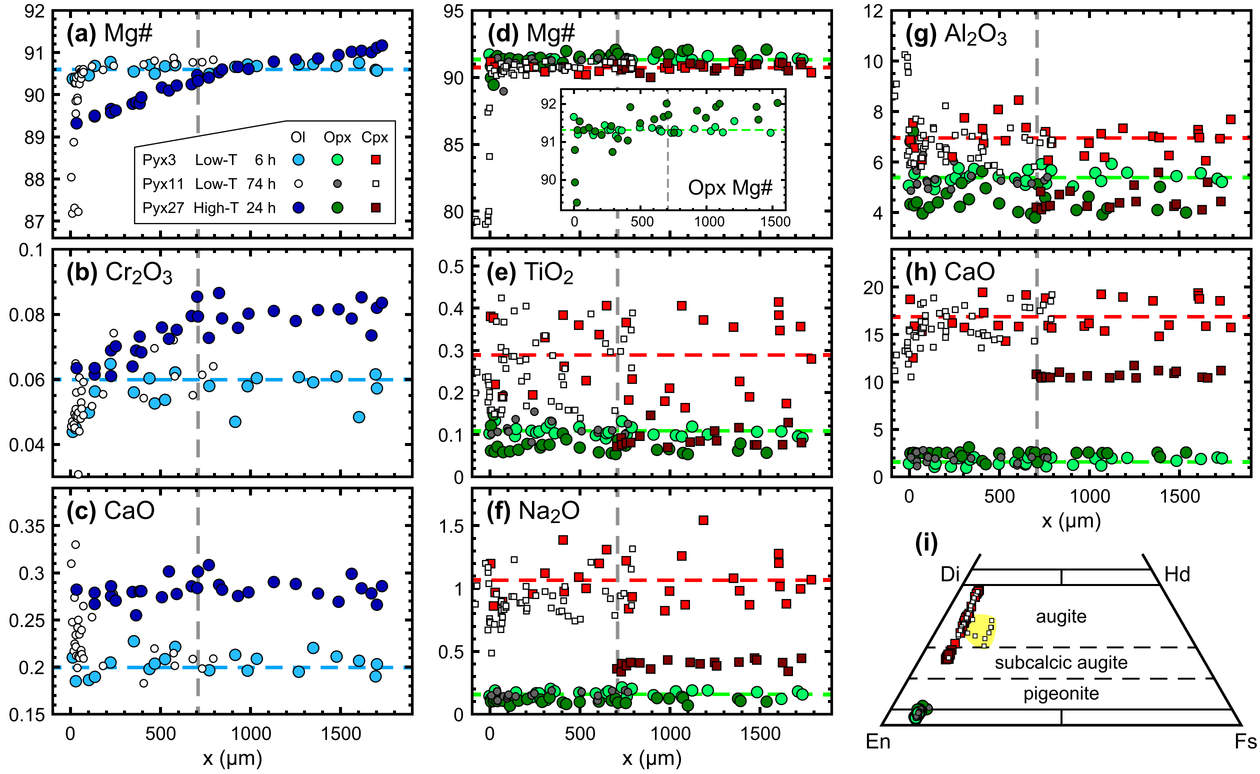

Fig. 7. Plots of oxide abundances (in wt%) and Mg# in olivine (**a**–**c**) and pyroxenes (**d**–**h**) as a function of distance away from the melt-rock interface (*x*) for representative experiments (Pyx3, Pyx11, and Pyx27). The dashed gray vertical lines mark the position of the harzburgite-lherzolite boundary in Pyx27. The dashed horizontal lines mark the average compositions of olivine (blue), orthopyroxene (green), and clinopyroxene (red) in the interior region of lherzolite from run Pyx3. Pyroxene compositions are plotted in the quadrilateral diagram in **i**. The yellow area in **i** shows the composition range of clinopyroxene on the melt side of interface in run Pyx11. Di: diopside, Hd: hedenbergite, En: enstatite, Fs: ferrosilite. (For interpretation of the references to colour in this figure legend, the reader is referred to the web version of this article.)

$$V = \frac{L}{2t} = \frac{k}{2\sqrt{t}} \tag{4b}$$

where k is the diffusive dissolution constant which is the slope of the linear regression line for each set of experiment in Fig. 4a. Using Eqs. (3) and (4) and estimated Θ and k, we calculate EBDC (D_f) of Al_2O_3, which is one of the major oxides in the melt that does not show uphill diffusion pattern in composition profiles from all the experiments (Fig. 5). The obtained k and EBDC for the short-duration experiments are listed in Table 3. These EBDC values are within the range defined by the diffusion coefficients in similar melt compositions at similar temperatures (Zhang et al., 2010 and references therein, Fig. S4).

The total thickness of orthopyroxene-rich layers in the high-temperature experiments increases approximately linearly as a function of the square root of time (Fig. 4b). The growth rates of the orthopyroxene-rich layer and pure orthopyroxenite, as characterized by the reaction constants $k_{opx\text{-}rich}$ and k_{opxite} can be estimated using Eq. (4) and our measured layer thickness in Fig. 4b. The results are summarized in Table 3. Overall, the growth rate of the orthopyroxene-rich layer is 1.9–6.6 times of the peridotite dissolution rate, whereas the growth rate of the pure

Table 3
Reaction constants and Al_2O_3 effective binary diffusion coefficient of the experiments.

Run series	T (°C)	k^a ($\mu m/s^{0.5}$)			EBDC^b ($\mu m^2/s$)
		Dissolution	Opx-rich	Opxite	
Pyx low-T	1300	0.13 ± 0.02	–	–	1.10
Pyx high-T	1375	1.18 ± 0.05	2.30 ± 0.32	–	24.02
26W	1425	1.50 ± 0.04	9.95 ± 0.89	0.32 ± 0.02	20.49
JW	1425	2.21 ± 0.08	4.39 ± 0.90	0.67 ± 0.001	60.56

[a] Diffusive dissolution or growth constant (±1 σ). Opx-rich: orthopyroxene-rich layers; opxite: orthopyroxenite.

[b] Effective binary diffusion coefficient of each series of experiment was calculated using Eqs. (3) and (4) and measurements from the relatively short duration experiments Pyx3, Pyx26, 26W01, and JW03.

orthopyroxenite is only 20–30% of the peridotite dissolution rate. Hence, orthopyroxene-rich harzburgite is expected to be more prevalent than pure orthopyroxenite as the product of eclogite-derived melt and peridotite reaction. Growth of orthopyroxenite in the JW experiments is twice as fast as that in the 26W experiments (Fig. 4b, Table 3). Using Fourier Transform Infrared Microscopy, we detected a small amount of water in the reacted melt (0.44 wt%) in the JW experiments. The water is derived from the breakdown of amphibole in the amphibole-

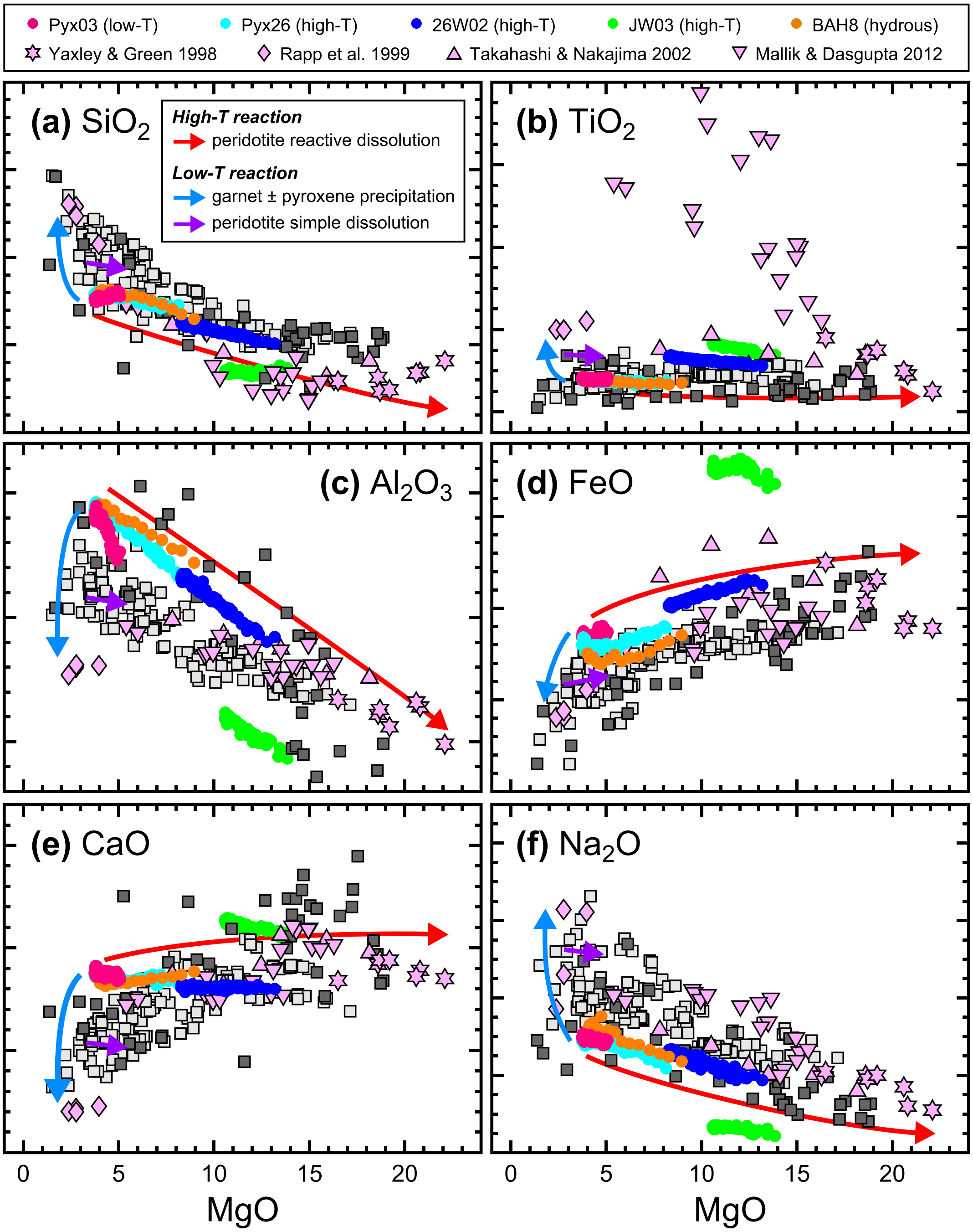

Fig. 8. Plots of oxide abundances (in wt%) versus MgO (in wt%) in melts obtained from representative dissolution experiments from this study, hydrous basaltic andesite and lherzolite reaction experiment (BAH8) from Wang et al. (2016), melt-rock reaction experiments from previous studies (Yaxley and Green, 1998; Rapp et al., 1999; Takahashi and Nakajima, 2002; Mallik and Dasgupta, 2012), and field observations from the NCC (same as those in Fig. 6). Red arrows mark the melt compositional variation caused by peridotite reactive dissolution during the high-T melt-rock reaction. Blue and purple arrows mark the melt compositional variations caused by precipitation of garnet ± pyroxene and simple dissolution of peridotite, respectively, during the low-T melt-rock reaction. (For interpretation of the references to colour in this figure legend, the reader is referred to the web version of this article.)

bearing garnet clinopyroxenite JG4-1 (Wang et al., 2013). The small amount of water may enhance the growth of orthopyroxenite at 2 GPa and 1425 °C, as demonstrated in Wang et al. (2016) through hydrous melt and peridotite reaction experiments.

4.3. Melt compositional variations in the melt-rock reaction experiments

Fig. 8 compares the compositions of melt obtained from representative melt-rock reaction experiments in this study with those from Yaxley and Green (1998), Rapp et al. (1999), Takahashi and Nakajima (2002), Mallik and Dasgupta (2012), and Wang et al. (2016). Compositional variation of melt produced in the reaction experiments mainly depends on the stating melt composition, melt-to-rock ratio, and the kinetics or style of melt-rock reaction. Compared with the previous experiments, run JW03 produced melts with significantly low SiO_2, Al_2O_3, and Na_2O contents, and high TiO_2, FeO, and CaO contents; the experiments of Mallik and Dasgupta (2012) produced melts with low SiO_2 content and high TiO_2 content. These are due to the specific starting melts used in these experiments. JG4-1 has low SiO_2, Al_2O_3, Na_2O, and high FeO, and the starting melts used in the experiments of Mallik and Dasgupta (2012) have low SiO_2 and high TiO_2 within the composition range of eclogite partial melts (Fig. S2).

Except the experiments from Rapp et al. (1999), which were run at a considerably low temperature (1100 °C) with respect to the high pressure (3.8 GPa), all the experiments produced melts with elevated MgO content. The experiments from Yaxley and Green (1998) produced the most MgO enriched melts. Such difference in reacted melt composition can be attributed to different kinetics of melt-rock reaction. Reaction kinetics in the high-temperature (1425–1550 °C) experiments of Yaxley and Green (1998) is similar to that in the high-T experiments from this study. High-Mg melts are produced by reactive dissolution of peridotite in the starting eclogite-derived melt. Compositions of melts from the experiments of Yaxley and Green (1998), Takahashi and Nakajima (2002), Mallik and Dasgupta (2012), and the high-T Pyx experiment from this study form continuous trends in Fig. 8 (red arrows). Composition of melt from hydrous basaltic andesite (Mont147 with 4 wt% H_2O) and lherzolite reaction experiment of Wang et al. (2016) also varies along this trend. In the oxide versus MgO diagrams, SiO_2, Al_2O_3, and Na_2O decrease, while FeO and CaO increase with MgO (red arrows in Fig. 8), i.e., the melts evolve towards peridotite composition (red arrow in Fig. 6).

Reaction kinetics in the low-temperature (1100 °C) experiments of Rapp et al. (1999) is similar to the low-T experiments in this study, in which the reaction is dominated by crystallization of garnet ± pyroxene with a small amount of peridotite dissolution. Crystallization of garnet ± pyroxene increases SiO_2, Ti_2O, and Na_2O, and decreases Al_2O_3, FeO, MgO, and CaO in reacting melt (blue arrows in Fig. 8), whereas dissolution of peridotite increases MgO (and thus Mg#) in reacting melt (purple arrows in Fig. 8). The effect of garnet precipitation on melt composition is facilitated by pressure and reaction time. In the 3.8 GPa experiments of Rapp et al. (1999), a significant amount of pyrope-rich garnet is precipitated at reaction front, so the reacted melts are distinctly high in SiO_2 and low in Al_2O_3 (Fig. 8). In the low-T Pyx experiments, the amount of garnet crystallization increases with time (Fig. 2(a and b)), which makes the composition of melt at the interface evolve towards quartz-normative (blue arrows in Fig. 6).

In summary, reactions between lherzolite and eclogite-derived melt in the low-T and high-T regimes have different effects on the mineralogy, reaction rate, equilibration time, and melt compositional variations. These melt-rock reaction processes place important constraints on how eclogite-derived melts interact physically and chemically with the surrounding peridotite in the lithospheric mantle.

5. GEOLOGICAL APPLICATIONS

High-Mg basalts and diorites and mantle xenoliths carried by these rocks have been investigated to infer spatial and temporal variations of melt-peridotite interaction in the NCC. The experimental results of this study have demonstrated different styles of melt-rock reaction. As an application, we compare the experimental results with the field observations from the Mesozoic igneous rocks and the mantle xenoliths from the NCC to assess the effects of different types of melt-peridotite interaction in modifying the lithospheric mantle beneath the NCC.

5.1. Survival of mantle xenoliths during transport in an eclogite-derived melt

Fragments of lithospheric mantle are frequently brought to the surface by eruptions of alkali basalts, kimberlites, and lamprophyres as xenoliths. By comparison, there are very few cases in which mantle xenoliths are entrained by siliceous magmas, in part due to the high viscosity of siliceous magmas and their large compositional difference from ultramafic mantle rocks. A rare exception is the prevalence of mantle xenoliths found in the Early Cretaceous high-Mg diorites from the Eastern Block and TNCO of the NCC (e.g., Huang and Xue, 1990; Chen and Zhou, 2005; Xu et al., 2008, 2010; Wang et al., 2018). These xenoliths are round in shape, $3 \times 2 \times 1\ cm^3$ to $8 \times 6 \times 4\ cm^3$ in size, and have a clear contact with the host diorites. An interesting question is under what condition these mantle xenoliths survive their transport in the dioritic melts.

The survival of a mantle xenolith in an ascending magma can be assessed through a convective dissolution calculation. Convective dissolution is characterized by a boundary layer where mass transfer is dominated by diffusion. Outside the convective boundary layer, the melt is well-mixed by convection. Thus, the rate of convective dissolution is expected to be greater than the rate of diffusive dissolution. According to Zhang et al. (1989) and Kerr (1995), rate of convective dissolution (m/s) can be expressed as

$$V = \frac{D_f}{\delta}\Theta \tag{5}$$

where D_f is the EBDC of a rate limiting component in the melt (Al_2O_3 in this study, m^2/s); Θ is the degree of undersaturation; and δ is thickness of the boundary layer (m). The calculation for thickness of the boundary layer in our case is outlined in Appendix 1. For the case in this study, the following parameters were used to calculate δ: xenolith density (ρ_s) of 3.2×10^3 kg/m^3, density (ρ_f, kg/m^3) and viscosity (μ, Pa·s) of the basaltic andesite (Mont147) calculated at a given temperature using the methods of Bottinga and Weill (1970) and Shaw (1972, assuming a pressure of 2 GPa), respectively, and temperature-dependent diffusivity (D_f) estimated from our EBDC of Al_2O_3 and those from the Zhang et al. (2010) using an Arrhenius equation (Fig. S4). The calculation suggests that in the ranges of temperature (T) from 700 °C to 1300 °C, degree of undersaturation (Θ) smaller than 0.5, and xenolith diameter (d) greater than 1×10^{-3} m, the Peclet number (Pe, Eq. (A.3)) is greater than 8000. Thus, δ takes the form of Eq. (A.8), and V (m) is independent of d:

$$V \approx \Theta\left(\frac{g(\rho_s - \rho_f)D_f{}^2}{18\mu}\right)^{1/3} \tag{6}$$

When diameter of the xenolith is smaller than 1×10^{-3} m, the dissolution rate is very fast. So, the survival time (s) of a xenolith can be simply defined as

$$t_s \approx \frac{d_0 - 1 \times 10^3}{V} \tag{7}$$

where d_0 is the initial diameter of a mantle xenolith (m).

Fig. 9a plots the survival time of a 20 cm diameter peridotite xenolith in a basaltic andesite melt as a function of magma temperature (T) and degree of undersaturation (Θ). Results of the calculation suggest that convective dissolution rate or survival time of the xenolith depends largely on temperature when the degree of undersaturation is larger than ~0.1. Degree of undersaturation (Θ) in the low-T dissolution experiments lies between 0.087 and 0.113. Within this range of Θ, a 20 cm diameter lherzolite xenolith entrained in an 1100 °C magma would completely dissolve in 17–24 years (Fig. 9b). If magma temperature is lower than 900 °C, the xenolith would survive for longer than hundreds of years (Fig. 9b). Dunite xenoliths are prevalent in diorites from the NCC. Although dissolution of dunite is not experimentally tested in this study, the degree of undersaturation of dioritic magma with respect to dunite is expected to be higher than the values obtained from our low-T experiments. Experimental study of olivine dissolution in a basaltic melt (50.2 wt% SiO_2, 13.6 wt% Al_2O_3) from Chen and Zhang (2008) obtained degree of undersaturation of 0.127–0.212 at 1270 °C. The high degree of undersaturation leads to a fast dissolution and short survival time of the xenolith, especially at high temperatures (e.g., >1100 °C, Fig. 9). Based on the geotherm constructed by equilibrium temperatures and pressures of garnet pyroxenites and lower crustal granulites (Huang and Xu, 2010) and the depths of seismic Moho (Chen et al., 2009), the temperature at crust-mantle boundary of the central and eastern NCC is around 800 °C. Thus, we suggest that a fast transport of the host dioritic magma to a shallow crustal

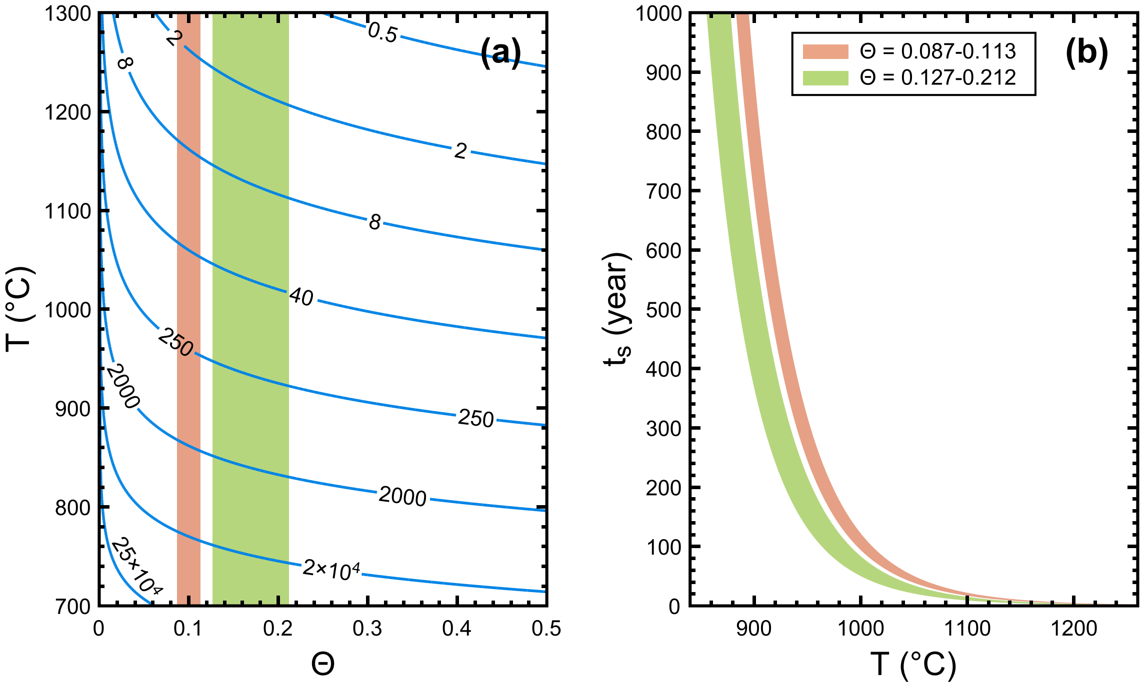

Fig. 9. Contour plot (**a**) of survival time (t_s, in year) of a 20 cm diameter xenolith in basaltic andesite (Mont147) as a function of the degree of undersaturation (Θ) and temperature of the host andesite (T). The light red field and the light green field denote the ranges of Θ measured in the low-T reaction experiments (Pyx3, Pyx10, and Pyx11) and experiments of olivine dissolution in basaltic melt at 1270 °C from Chen and Zhang (2008), respectively. Within these ranges, the calculated survival time is plotted as a function of temperature of host magma in **b**. (For interpretation of the references to colour in this figure legend, the reader is referred to the web version of this article.)

magma chamber is necessary to secure the survival of its entrained mantle xenoliths. The prevalence of NCC mantle xenoliths in diorites is in accordance with the hypothesis that the late Mesozoic NCC lithospheric mantle was thin and had a high geotherm (e.g., Menzies and Xu, 1998; Xu, 2001; Zheng et al., 2007). A thin lithospheric mantle helps to reduce the transport time for dioritic magmas from the high temperature mantle to the cold crust.

5.2. Styles of reaction between peridotite and eclogite-derived melt in the NCC lithospheric mantle

Orthopyroxene-rich harzburgite, orthopyroxenite-veined harzburgite, and orthopyroxenite-veined dunite are found as mantle xenoliths from the central and eastern NCC, and they are interpreted as products of interaction between the ancient lithospheric mantle and siliceous melts (e.g., Chen and Zhou, 2005; Xu et al., 2008, 2010; Wang et al., 2018). Results of our experiments demonstrated that the melt-rock reaction at high temperature when the peridotite is partially molten can readily produce orthopyroxene-rich lithologies. A possible location where such reaction takes place is at the lithosphere-asthenosphere boundary. The orthopyroxene-rich harzburgites from Hebi (Zheng et al., 2001; Sun et al., 2012; Tang et al., 2013) and Fuxin (Zheng et al., 2007) are likely formed by the high-T reaction. Wang et al. (2016) has demonstrated experimentally that orthopyroxenite veins in peridotites can be formed by reaction of peridotite with hydrous melts. Presence of hydrous minerals is a strong evidence of hydrous melt-rock reaction (Chen and Zhou, 2005; Xu et al., 2008, 2010; Wang et al., 2018).

Fig. 11 displays modal abundances of peridotites from ancient cratonic lithospheric mantle (NCC and Kaapvaal craton), deep oceanic lithospheric mantle (xenoliths in basalts from Hawaii and Tahiti), and shallow oceanic lithospheric mantle (abyssal and ophiolitic peridotites). Compared with peridotites from oceanic lithospheric mantle, the Hebi, Fuxin, and Kaapvaal peridotites are depleted in clinopyroxene, and a significant portion of them are enriched (>25%) in orthopyroxene. Modal variation of these orthopyroxene-rich peridotites follows the trends similar to those observed in the high-T reaction experiments (cyan, green, and blue arrows in Fig. 11a). Thus, orthopyroxene enrichment by reaction with eclogite-derived melts in the high-T regime is likely common during the evolution of ancient cratonic lithospheric mantle (Kelemen et al., 1998). Modal compositions of the Fushan, Tietonggou, and Jinling xenoltihs entrained by high-Mg diorites are comparable to those observed in the hydrous melt-peridotite reaction experiments of Wang et al. (2016, pink areas in Fig. 11a). This underscores the importance of hydrous melt in modifying the composition of lithospheric mantle in these regions. Lambart et al. (2012) demonstrated thermodynamically that reactions between pyroxenite-derived basaltic melts and peridotite at 1400 °C and 2.5 GPa enriches the mantle peridotite with clinopyroxene (dashed orange arrows in Fig. 11b). Such reaction results are consistent with the modal compositional variation of peridotites from deep oceanic lithospheric mantle. Experiments of Daines and Kohlstedt (1994) and Morgan and Liang (2003, 2005) showed that reactions between basaltic melts and partially molten peridotites at low pressures (0.3–1 GPa) produce orthopyroxene-poor harzburgite or dunite (dashed light green arrow in Fig. 11b). Such reactions beneath mid ocean ridges contribute to the depletion in pyroxene in shallow oceanic lithospheric mantle.

Based on our measured growth rate, reaction between peridotite and a basaltic andesite melt (JG1-26) at 1425 °C and 2 GPa can produce a ~170 m thick orthopyroxene-rich harzburgite zone surrounded by a ~6 m thick orthopyroxenite in 10 million year (Fig. 10). These estimations are lower bounds as they are based on the diffusive dissolution experiments. In a more realistic case, where the reacting melt percolates through the partially molten peridotite, the formation rates of orthopyroxene-rich lithologies would be higher. At tectonically active regions of the lithospheric mantle (Fig. 12a), the reactive dissolution may provide pathways for infiltration of the eclogite-derived melt (Fig. 12b). When volume of the reacting melt is limited, orthopyroxene precipitation would slow down the reaction by hindering melt infiltration. This effect is demonstrated by the long-duration experiment Pyx20 (Fig. 3) and the melt-deficient reaction experiments in Yaxley and Green (1998). Presence of water facilitates formation of orthopyroxenite during peridotite and siliceous melt reaction (Wang et al., 2016). Since water depolymerizes silicate melt and enhances cation diffusion, we expect the growth rate of orthopyroxenite in hydrous melt to be faster than that in the high-T anhydrous reaction experiments reported in this study. Further quantification of these more realistic but complicated problems requires the knowledge of permeability and rheology of the peridotite and orthopyroxene-rich lithology, which is beyond the scope of the present study.

When the eclogite-derived melts infiltrate into the shallow part the lithospheric mantle where temperature is low or water in melts is depleted by diffusive exchange with

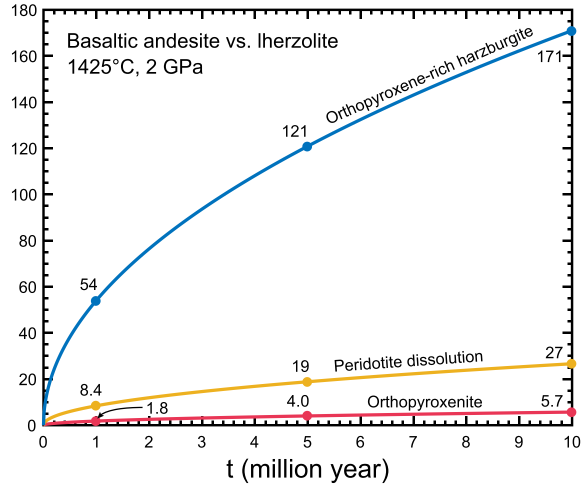

Fig. 10. Plot of peridotite dissolution distance and growths of orthopyroxene-rich lithologies as a function of time (curves). The distances and thicknesses at 1 Ma, 5 Ma, and 10 Ma are marked with spots.

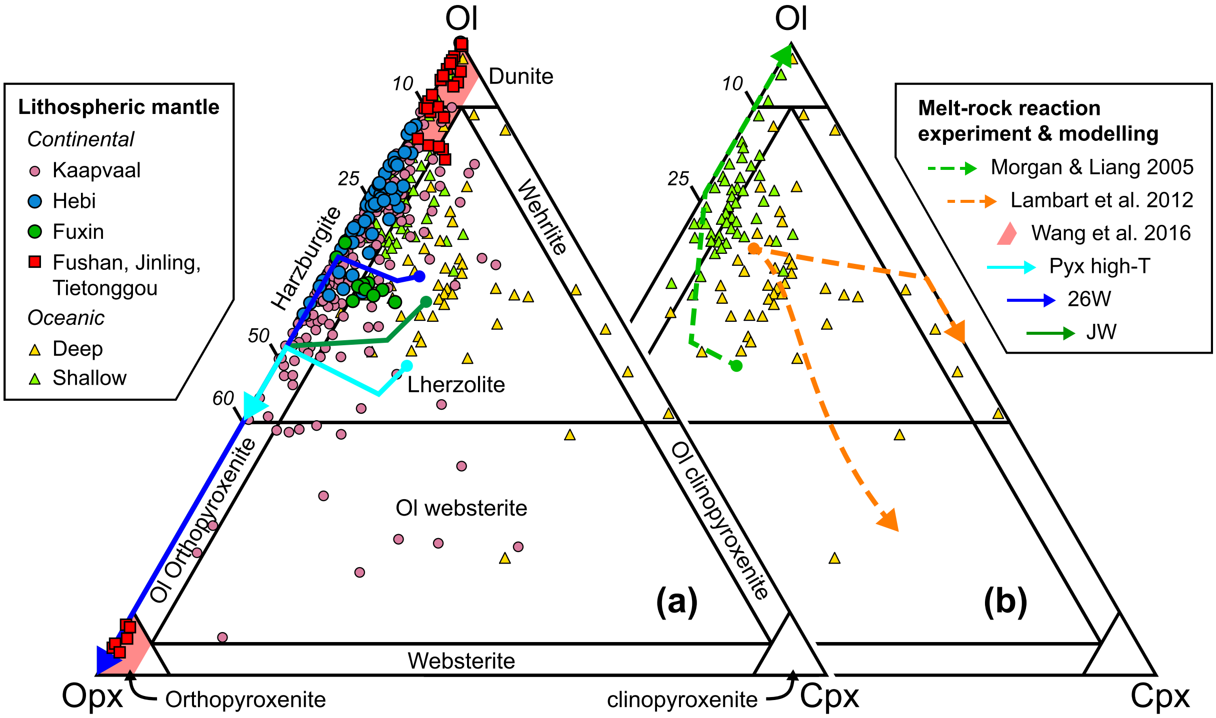

Fig. 11. Petrological classification of peridotite and pyroxenite on the olivine-orthopyroxene-clinopyroxene triangle projection. Modal compositional variations obtained from dissolution experiments and thermodynamic modelling are compared with those of peridotites from cratonic lithospheric mantle and oceanic lithospheric mantle. The experiments include the high-T reaction experiments from this study (solid arrows in **a**), hydrous melt-peridotite reaction experiments from Wang et al. (2016, magenta areas in **a**), and basalt-peridotite reaction experiment (run Lherzdis4) from Morgan and Liang (2005, dashed light green arrow in **b**). The modelling is melting peridotites impregnated by 0–100% of pyroxenite-derived melts at 2.5 GPa and 1400 °C conducted by Lambart et al. (2012, dashed orange arrow in **b**). Cratonic lithospheric mantle peridotites are xenoliths from Hebi (Zheng et al., 2001; Tang et al., 2013), Fuxin (Zheng et al., 2007), Fushan (Xu et al., 2010), Jiling and Tiegongou (Xu et al., 2008), NCC, and xenoliths entrained by kimberlites from the Kaapvaal craton. Deep oceanic lithospheric mantle peridotites are xenoliths entrained by basalts from ocean islands (Hawaii and Tahiti), and shallow oceanic lithospheric mantle peridotites are abyssal and ophiolitic peridotites. The Kaapvaal and oceanic data are from compilation of Fan et al. (2000). Numbers in italic indicate orthopyroxene modal abundance.

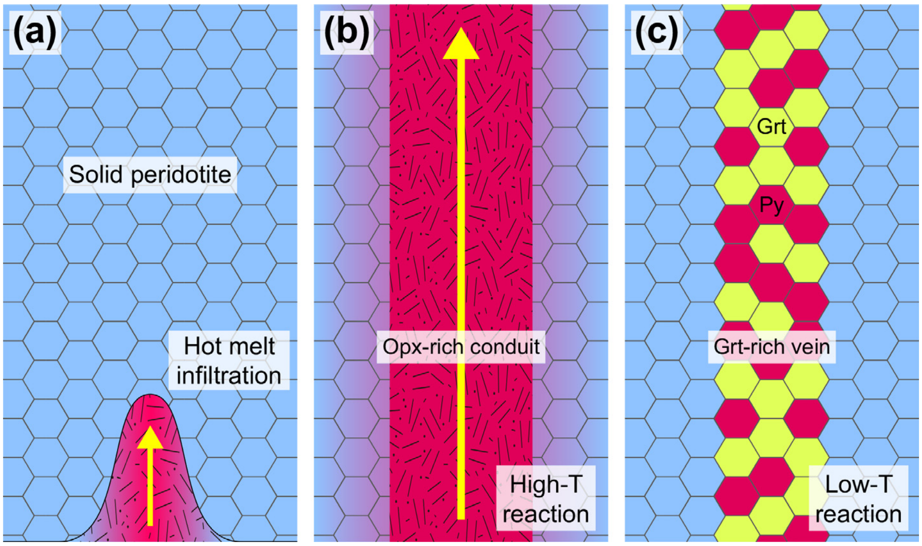

Fig. 12. Schematic illustration of eclogite-derived melt and peridotite interactions in the lithospheric mantle beneath the NCC. **a**. Eclogite-derived melt infiltrates peridotite in lithospheric mantle near the lithosphere-asthenosphere boundary, promoting partial melting of the peridotite. **b**. The high-T reaction between the partially molten peridotite and the melt produces an orthopyroxene-rich conduit. **c**. Within the subsolidus lithospheric mantle, the low-T reaction results in a garnet-bearing or garnet-rich vein (garnet pyroxenite or garnetite) in the host peridotite. Opx: orthopyroxene, Grt: garnet, Py: pyroxene. See text for discussion.

the ambient mantle, the low-T regime dominates the reaction. Reactive crystallization can produce garnet-bearing and/or garnet-rich lithologies, such as garnet pyroxenite, high-Mg granulite, and garnetite. One example is the suite of spinel lherzolite, garnet pyroxenite, and granulite xenoliths from Hannuoba, northern TNCO (Liu et al., 2005). Garnet and clinopyroxene are crystallized by reaction similar to that in the low-T experiments in this study, and orthopyroxene is precipitated when composition of the reacting melt is depleted by the reaction (Rapp et al., 1999), forming the garnet pyroxenite (Fig. 12c). The high-Mg granulite is formed by crystallization of the reacted melt. Garnetite and garnet-rich pyroxenite (23–53% garnet) were found as veins in garnet peridotites from the Sulu ultrahigh pressure terrane (Su et al., 2019), a Triassic orogen formed by subduction of the Yangtze Craton beneath the NCC (Li et al., 1993). These veins (~2 cm in width) contain large garnet porphyroblasts (3–10 mm in diameter) with high Mg# (74.2–77.4). Fine-grained garnet, pyroxene, olivine, and phlogopite occur interstitial to the large garnets. As demonstrated in Section 4.1, high pressure favors garnet crystallization during the low-T reaction. The Sulu garnet-rich veins could be formed in the low-T regime in the subsolidus lithospheric mantle following a process similar to that described in this study.

5.3. Origin of compositional variation of Mesozoic high-Mg igneous rocks from the NCC

Melt-rock reaction affects not only lithology and mineralogy of the lithospheric mantle, but also the geochemistry of magma. Here we assess the effect of melt-rock reaction on the compositional variation of late Mesozoic high-Mg igneous rocks from the NCC. Figs. 6 and 8 compare the compositions of the NCC high-Mg igneous rocks (Zhang et al., 2002; Gao et al., 2004; Pei et al., 2004; Xu et al., 2006; Huang et al., 2008; Yang et al., 2006, 2008; Qian and Hermann, 2010; Xu et al., 2009; Wang et al., 2011; Chen et al., 2013) with those of the melt obtained from melt-rock reaction experiments (Yaxley and Green, 1998; Rapp et al., 1999; Takahashi and Nakajima, 2002; Mallik and Dasgupta, 2012; Wang et al., 2016, and this study). Also plotted are compositions of the high-Mg granulites from Hannuoba (Liu et al., 2001, 2005; Zhou et al., 2002). Compositional variation of the NCC samples broadly overlap the trend established by reacted melts from the high-T melt-rock reaction experiments (red arrows in Figs. 6 and 8). This suggest that the NCC high-Mg igneous rocks can be formed by assimilation of peridotite into eclogite-derived melts in the high-T regime. However, the high-T reaction trend has lower SiO_2, Na_2O contents, and higher CaO, Al_2O_3, FeO contents than the NCC rocks (Fig. 8). These differences may be explained by processes similar to those observed in the low-T reaction experiments. Garnet crystallization increases SiO_2 and Na_2O contents and reduces Al_2O_3 content in the reacted melts, and clinopyroxene crystallization reduces CaO content in the melts (Fig. 8). The garnet crystallization is supported by the strong enrichment of light rare earth element relative to heavy rare earth elements in the high-Mg igneous rocks in NCC (e.g., Yang et al., 2006, 2008; Qian and Hermann, 2010; Xu et al., 2009; Wang et al., 2011; Chen et al., 2013). The high-T and low-T reactions that take place at different depths in the lithospheric mantle jointly contribute the geochemical variations of the high-Mg igneous rocks.

6. CONCLUSIONS

Dissolution and growth rates of lithologies and melt compositional variations during lherzolite and eclogite-derived melt reaction are examined experimentally at 2 GPa using the dissolution couple method. Results of the experiments and those from previous studies conducted at higher pressures (up to 3.8 GPa) provide important insights into the mechanism and style of melt-peridotite interaction in the lithospheric mantle beneath the NCC. The main conclusions of this study can be summarized as follows:

1. Reaction between lherzolite and eclogite-derived melts can be divided into two regimes: the low-T regime when the reacting lherzolite is subsolidus and the high-T regime when the lherzolite is partially molten.
2. The low-T reaction is characterized by simple dissolution with a slow dissolution rate. Garnet and clinopyroxene are precipitated at the melt-peridotite interface. High pressures facilitate garnet precipitation, and high silica contents in melt promote orthopyroxene crystallization. The low-T reaction forms garnet-rich lithologies, such as garnet pyroxenite and garnetite. The high-T reaction is characterized by reactive dissolution with high dissolution and growth rates. Preferential dissolution of olivine and precipitation of orthopyroxene result in orthopyroxene-rich lithologies, such as orthopyroxene-rich harzburgite and orthopyroxenite.
3. The low-T reaction generally produces melts with increased SiO_2, Na_2O, and decreased Al_2O_3, FeO, and CaO, whereas the high-T reaction produces melt with increased MgO, FeO, CaO, and Mg#, and decreased SiO_2, Al_2O_3, and Na_2O.
4. A necessary condition for mantle xenoliths to survive in a dioritic host magma is a fast transport of the magma into a shallow crustal magma chamber. The prevalence of mantle xenoliths in the NCC high-Mg diorites is attributed to the thin lithospheric mantle in the late Mesozoic.
5. The ancient NCC lithospheric mantle experienced both the high-T and low-T reactions with eclogite-derived melts. The high-T reaction produces orthopyroxene-rich harzburgite, orthopyroxenite-veined harzburgite, and orthopyroxenite-veined dunite. The low-T reaction produces garnet pyroxenite, high-Mg granulite, and garnetite.
6. Interactions between melts derived from delaminated lower crust in the high-T regime and the low-T regime jointly form the geochemical features of late Mesozoic high-Mg igneous rocks from the NCC.

ACKNOWLEDGEMENTS

We wish to thank the three anonymous reviewers for their detailed and constructive reviews which helped to improve this manuscript. We also thank Fangzhen Teng and Sonja Aulbach for their editorial handling. This work was supported by grants from National Natural Science Foundation of China (41602043 and 91858211) and Key Basic Research Program of China (2015CB856101), grants from US National Science Foundation (EAR-0510606, EAR-120076 and EAR-1624516), and a Brown University dissertation fellowship (to MLC).

APPENDIX A. THICKNESS OF COMPOSITIONAL BOUNDARY LAYER AROUND A SPHERICAL XENOLITH DURING CONVECTIVE DISSOLUTION

The thickness of the convective boundary layer around a moving sphere of diameter d in an effectively infinite fluid reservoir can be estimated using the approximated expression (Cussler, 1997):

$$\delta = \frac{d}{Sh} \tag{A.1}$$

$$Sh \approx 1 + (1 + Pe)^{1/3} \tag{A.2}$$

$$Pe = \frac{Ud}{D_f} \tag{A.3}$$

$$U = \frac{g(\rho_s - \rho_f)d^2}{18\mu} \tag{A.4}$$

$$Re = \frac{Ud\rho_f}{\mu} \tag{A.5}$$

where ρ_f and ρ_s are density of the magma and density of the solid, respectively; μ is the viscosity of the magma; U is the Stokes settling velocity of the spherical particle; Sh is the Sherwood number; Pe is the Peclet number; and Re is the Reynolds number. The dimensionless Sherwood number is a measure of the rate of total mass transfer relative to the rate of diffusive mass transfer (Cussler, 1997). The Stokes law (Eq. (A.4)) is applicable when the Reynolds number is smaller than 1. If Re is greater than 1, a drag coefficient C_D (Clift et al., 1978) is introduced to correct U (Zhang and Xu, 2003):

$$C_D = \frac{24}{Re}(1 + 0.15Re^{0.687}) \tag{A.6}$$

$$U = \sqrt{\frac{4gd(\rho_s - \rho_f)}{3\rho_f C_D}} \tag{A.7}$$

When Peclet number is great (i.e., $Pe \gg 1$), which mean that the forced convection is strong, the boundary layer thickness

$$\delta \approx \left(\frac{18\mu D_f}{g(\rho_s - \rho_f)}\right)^{1/3} \tag{A.8}$$

becomes independent of d (Kerr, 1995).

APPENDIX B. SUPPLEMENTARY MATERIAL

Supplementary data to this article can be found online at https://doi.org/10.1016/j.gca.2019.09.022.

REFERENCES

Anderson D. A. (2006) Speculations on the nature and cause of mantle heterogeneity. *Tectonophysics* **146**, 7–22.

Beck S. L. and Zandt G. (2002) The nature of orogenic crust in central Andes. *J. Geophys. Res.* **107**, B10.

Bottinga Y. and Weill D. F. (1970) Densities of liquid silicate systems calculated from partial molar volumes of oxide components. *Am. J. Sci.* **269**, 169–182.

Carlson R. W., Irving A. J. and Hearn, Jr., B. C. (1999) *Chemical and isotopic systematics of peridotite xenoliths from the Williams kimberlite, Montana: clues to processes of lithosphere formation, modification and destruction*. Red Roof Design, Cape Town, pp. 90–98.

Chen B., Jahn B.-M. and Suzuki K. (2013) Petrological and Nd-Sr-Os isotopic constraints on the origin of high-Mg adakitic rocks from the North China Craton: tectonic implications. *Geology* **41**, 91–94.

Chen L. H. and Zhou X. H. (2005) Subduction-related metasomatism in the thinning lithosphere: evidence from a composite dunite–orthopyroxenite xenolith entrained in Mesozoic Laiwu high-Mg diorite, North China Craton. *Geochem. Geophys. Geosys.* **6**, Q06008.

Chen L., Cheng C. and Wei Z. G. (2009) Seismic evidence for significant lateral variations in lithospheric thickness beneath the central and western North China Craton. *Earth Planet. Sci. Lett.* **286**, 171–183.

Chen Y. and Zhang Y. (2008) Olivine dissolution in basaltic melt. *Geochim. Cosmochim. Acta* **72**, 4756–4777.

Chen Y. and Zhang Y. (2009) Clinopyroxene dissolution in basaltic melt. *Geochim. Cosmochim. Acta* **73**, 5730–5747.

Clift R., Grace J. R. and Weber M. E. (1978) *Bubbles, Drops, and Particles*. Academic Press, New York, p. 380.

Cooper A. R. (1968) The use and limitations of the concept of an effective binary diffusion coefficient for multicomponent diffusion. In *Mass Transport in Oxides* (eds. J. B. Wachtman and A. D. Franklin). NBS Special Publ., pp. 79–84.

Cussler E. L. (1997) *Diffusion Mass Transfer in Fluid Systems*. Cambridge University Press, Cambridge.

Daines M. J. and Kohlstedt D. L. (1994) The transition from porous to channelized flow due to melt/rock reaction during melt migration. *Geophys. Res. Lett.* **21**, 145–148.

Fan W. M. and Menzies M. A. (1992) Destruction of aged lower lithosphere and accretion of asthenosphere mantle beneath eastern China. *Geotectonica Metallogenia.* **16**, 171–180.

Fan W. M., Zhang H. F., Baker J., Jarvis K. E., Mason P. R. D. and Menzies M. A. (2000) On and off the North China Craton: where is the Archaean keel? *J. Petrol.* **41**, 933–950.

Gao S., Rudnick R. L., Carlson R. W., McDonough W. F. and Liu Y. S. (2002) Re–Os evidence for replacement of ancient mantle lithosphere beneath the North China Craton. *Earth Planet. Sci. Lett.* **198**, 307–322.

Gao S., Rudnick R. L., Xu W.-L., Yuan H.-L., Liu Y.-S., Walker R.-J., Puchtel I. S., Liu X.-M., Huang H., Wang X.-R. and Yang J. (2008) Recycling deep cratonic lithosphere and generation of intraplate magmatism in the North China Craton. *Earth Planet. Sci. Lett.* **270**, 41–53.

Gao S., Rudnick R. L., Yuan H.-L., Liu X.-M., Liu Y.-S., Xu W.-L., Ayers J., Wang X.-C. and Wang Q.-H. (2004) Recycling lower continental crust in the North China craton. *Nature* **432**, 892–897.

Huang F. and Xue S. (1990) The discovery of the mantle-derived ultramafic xenoliths in Handan Xingtai intrusive complex and their mineralogical-geochemical characteristics. *Acta Petrol. Sin.* **6**, 40–45 (In Chinese with English abstract).

Huang F., Li S. G., Dong F., He Y. S. and Chen F. K. (2008) High-Mg adakitic rocks in the Dabie orogen, central China: implications for foundering mechanism of lower continental crust. *Chem. Geol.* **255**, 1–13.

Huang X. L. and Xu Y. G. (2010) Thermal state and structure of the lithosphere beneath eastern China: a synthesis on basalt-borne xenoliths. *J. Earth Sci.* **21**, 711–730.

Kelemen P. B., Hart S. R. and Bernstein S. (1998) Silica enrichment in the continental upper mantle via melt/rock reaction. *Earth Planet. Sci. Lett.* **164**.

Kerr R. C. (1995) Convective crystal dissolution. *Contrib. Mineral. Petrol.* **121**, 237–246.

Kobussen A. F., Griffin W. L., O'Reilly S. Y. and Shee S. Y. (2008) Ghosts of lithospheres past: imaging an evolving lithospheric mantle in southern Africa. *Geology* **36**, 515–518.

Lambart S., Laporte D., Provost A. and Schiano P. (2012) Fate of pyroxenite-derived melts in the peridotitic mantle: thermodynamic and experimental constraints. *J. Petrol.* **53**, 451–476.

Li S., Xiao Y., Liou D., Chen Y., Ge N., Zhang Z., Sun S., Cong B., Zhang R., Hart S. R. and Wang S. (1993) Collision of the North China and Yangtze blocks and formation of coesite-bearing eclogites: timing and processes. *Chem. Geol.* **109**, 89–111.

Liang Y. (2000) Dissolution in molten silicates: effects of solid solution. *Geochim. Cosmochim. Acta* **64**, 1617–1627.

Liang Y. (1999) Diffusive dissolution in ternary systems: analysis with applications to quartz and quartzite dissolution in molten silicates. *Geochim. Cosmochim. Acta* **63**, 3983–3995.

Liang Y. (2003) Kinetics of crystal-melt reaction in partially molten silicates: 1. Grain scale processes. *Geochem. Geophys. Geosyst.* **4**, 1045.

Liu Y. S., Gao S., Lee C. T. A., Hu S. H., Liu X. M. and Yuan H. L. (2005) Melt-peridotite interactions: links between garnet pyroxenite and high-Mg# signature of continental crust. *Earth Planet. Sci. Lett.* **234**, 39–57.

Liu Y., Gao S., Jin S., Hu S., Sun M., Zhao Z. and Feng J. (2001) Geochemistry of lower crustal xenoliths from Neogene Hannuoba basalt, north china craton: implications for petrogenesis and lower crustal composition. *Geochim. Cosmochim. Acta* **65**, 2589–2604.

Lo Cascio M. (2008) Kinetics of Partial Melting and Melt-Rock Reaction in the Earth's Mantle. In *Ph.D. Thesis*. Brown University. https://doi.org/10.7301/Z0SF2TK0.

Lo Cascio M., Liang Y., Shimizu N. and Hess P. C. (2008) An experimental study of the grain-scale processes of peridotite melting: implications for major and trace element distribution during equilibrium and disequilibrium melting. *Contrib. Mineral. Petrol.* **155**, 1–16.

Lo Cascio M., Liang Y. and Hess P. C. (2004) Grain-scale processes during isothermal-isobaric melting of lherzolite. *Geophys. Res. Lett.* **31**, L16605.

Mallik A. and Dasgupta R. (2012) Reaction between MORB-eclogite derived melts and fertile peridotite and generation of ocean island basalts. *Earth Planet. Sci. Lett.* **329–330**, 97–108.

Menzies M. A. and Xu Y. G. (1998) Geodynamics of the North China Craton. In *Mantle Dynamics and Plate Interactions in East Asia* (eds. M. F. J. Flower, S.-L. Chung, C.-H. Lo and T.-Y. Lee). Am. Geophy. Union, Washington, DC Geodyn. Ser., pp. 155–165.

Menzies M. A., Zhang M. and Fan W. M. (1993) Palaeozoic and Cenozoic lithoprobes and the loss of >120 km of Archaean lithosphere Sino-Korean Craton China. In *Magmatic Processes and Plate Tectonics* (eds. H. M. Prichard, T. Alabaster, N. B. W. Harris and C. R. Neary). Geological Society of London, pp. 71–81.

Menzies M., Xu Y. G., Zhang H. F. and Fan W. M. (2007) Integration of geology, geophysics and geochemistry: a key to understanding the North China Craton. *Lithos* **96**, 1–21.

Morgan Z. and Liang Y. (2003) An experimental and numerical study of the kinetics of harzburgite reactive dissolution with applications to dunite dike formation. *Earth Planet. Sci. Lett.* **214**, 59–74.

Morgan Z. and Liang Y. (2005) An experimental study of the kinetics of lherzolite reactive dissolution with applications to melt channel formation. *Contrib. Mineral. Petrol.* **150**, 369–385.

Niu Y. L. (2005) Generation and evolution of basaltic magmas: some basic concepts and a new view on the origin of Mesozoic-Cenozoic basaltic volcanism in Eastern China. *Geol. J. China Univ.* **11**, 9–46.

O'Hara M. J. (1968) The bearing of phase equilibria studies in synthetic and natural systems on the origin and evolution of basic and ultrabasic rocks. *Earth Sci. Rev.* **4**, 69–133.

Pei F., Xu W., Wang Q., Wang D. and Lin J. (2004) Mesozoic basalt and mineral chemistry of the mantle-derived xenocrysts in Feixian, Western Shandong, China: constraints on nature of mesozoic lithospheric mantle. *Geol. J. China Univ.* **10**, 88–97 (in Chinese with English abstract).

Qian Q. and Hermann J. (2010) Formation of high-Mg diorites through assimilation of peridotite by monzodiorite magma at crustal depths. *J. Petrol.* **51**, 1381–1416.

Rapp R. P., Shimizu N., Norman M. D. and Applegate G. S. (1999) Reaction between slab-derived melts and peridotite in the mantle wedge: experimental constraints at 3.8 GPa. *Chem. Geol.* **160**, 335–356.

Rudnick R. L. and Fountain D. M. (1995) Nature and composition of the continental crust: a lower crustal perspective. *Rev. Geophys.* **33**, 267–309.

Santosh M. (2010) Assembling North China Craton within the Columbia supercontinent: the role of double-sided subduction. *Precambrian Res.* **178**, 149–167.

Shaw H. R. (1972) Viscosities of magmatic silicate liquids: an empirical method of prediction. *Am. J. Sci.* **272**, 870–893.

Su B., Chen Y., Guo S., Chen S. and Li Y. B. (2019) Garnetite and pyroxenite in the mantle wedge formed by slab-mantle interactions at different melt/rock ratios. *J. Geophys. Res. Solid Earth* **124**. https://doi.org/10.1029/2019JB017347.

Sun J., Liu C. Z., Wu F. Y., Yang Y. H. and Chu Z. Y. (2012) Metasomatic origin of clinopyroxene in archean mantle xenoliths from Hebi, North China Craton: Trace-element and Sr-isotope constraints. *Chem. Geol.* **328**, 123–136.

Takahashi E. and Nakajima K. (2002) Melting process in the Hawaiian plume: an experimental study. In *Hawaiian Volcanoes: Deep Underwater Perspectives, Geophysical Monograph 128* (eds. E. Takahashi, P. W. Lipman, M. Garcia, J. Naka and S. Aramaki). American Geophysical Union, Washington, DC, pp. 403–418.

Tang Y. J., Zhang H. F., Ying J. F., Su B. X., Chu Z. Y., Xiao Y. and Zhao X. M. (2013) Highly heterogeneous lithospheric mantle beneath the central zone of the north china craton evolved from archean mantle through diverse melt refertilization. *Gondwana Res* **23**, 130–140.

Wang C., Liang Y., Xu W. and Dygert N. (2013) Effect of melt composition on basalt and peridotite interaction: laboratory dissolution experiments with applications to mineral compositional variations in mantle xenoliths from the North China Craton. *Contrib. Mineral. Petrol.* **166**, 1469–1488.

Wang C., Xu W., Wang F. and Yang D. (2011) Petrogenesis of the early cretaceous Xi'anli hornblende-gabbros from the Southern Taihang Mountains: evidence from zircon U-Pb geochronology, Hf isotope and whole-rock geochemistry. *Earth Sci. J. China Univ. Geosci.* **36**, 471–482 (in Chinese with English abstract).

Wang C., Xu W., Yang D., Liu Y., Pei F., Li Q. and Zhou Q. (2018) Olivine oxygen isotope evidence for intracontinental recycling of delaminated continental crust. *Geochem. Geophys. Geosys.* **19**, 1913–1924.

Wang C., Liang Y., Dygert N. and Xu W. (2016) Formation of orthopyroxenite by reaction between peridotite and hydrous basaltic melt: an experimental study. *Contrib. Mineral. Petrol.* **171**, 77.

Watson E. B. (1982) Basalt contamination by continental crust: some experiments and models. *Contrib. Mineral. Petrol.* **80**, 73–87.

Wu F. Y., Yang J. H., Xu Y. G., Wilde S. A. and Walker R. J. (2018) Destruction of the North China Craton in the Mesozoic. *Annu. Rev. Earth Planet. Sci.* **47**, 173–195.

Xu W., Hergt J. M., Gao S., Pei F., Wang W. and Yang D. (2008) Interaction of adakitic melt-peridotite: implications for the high-Mg# signature of Mesozoic adakitic rocks in the eastern North China Craton. *Earth Planet. Sci. Lett.* **265**, 123–137.

Xu W., Gao S., Yang D., Pei F. and Wang Q. (2009a) Geochemistry of eclogite xenoliths in Mesozoic adakitic rocks from Xuzhou-Suzhou area in central China and their tectonic implications. *Lithos* **107**, 269–280.

Xu W., Wang Q., Wang D., Guo J. and Pei F. (2006) Mesozoic adakitic rocks from the Xuzhou-Suzhou area, eastern China: evidence for partial melting of delaminated lower continental crust. *J. Asian Earth Sci.* **27**, 454–464.

Xu W., Yang D., Gao S., Pei F. and Yu Y. (2010) Geochemistry of peridotite xenoliths in Early Cretaceous high-Mg# diorites from the Central Orogenic Block of the North China Craton: the nature of Mesozoic lithospheric mantle and constraints on lithospheric thinning. *Chem. Geol.* **270**, 257–273.

Xu W., Yang D., Pei F. and Yu Y. (2009b) Petrogenesis of Fushan high-Mg# diorites from the southern Taihang Mts. in the central North China Craton: resulting from interaction of peridotite—melt derived from partial melting of delaminated lower continental crust. *Acta Petrol. Sin.* **25**, 1947–1961 (In Chinese with English abstract).

Xu Y. G. (2001) Thermo-tectonic destruction of the archaean lithospheric keel beneath the Sino-Korean craton in china: evidence, timing and mechanism. *Chem. Earth, Part A Solid Earth Geod.* **26**, 747–757.

Xu Y. G., Huang X. L., Ma J. L., Iizuka Y., Xu J. F., Wang Q. and Wu X.-Y. (2004) Crust-mantle interaction during the tectono-thermal reactivation of the North China Craton: constraints from SHRIMP zircon U-Pb chronology and geochemistry of Mesozoic plutons from western Shandong. *Contrib. Miner. Petrol.* **147**, 750–767.

Yang C. H., Xu W. L., Yang D. B., Wang W., Wang W. D. and Liu J. M. (2008) Petrogenesis of Shangyu gabbro-diorites in western Shandong: geochronological and geochemical evidence. *Sci. China Ser. D: Earth Sci.* **51**, 481–492.

Yang C., Xu W., Yang D., Liu C., Liu X. and Hu Z. (2006) Petrogenesis of the Mesozoic high-Mg diorites in west Shandong: evidence from chronology and petro-geochemistry. *Earth Sci. J. China Univ. Geosci.* **31**, 81–92 (in Chinese with English abstract).

Yaxley G. M. and Green D. H. (1998) Reactions between eclogite and peridotite: Mantle refertilisation by subduction of oceanic crust. *Schweiz. Mineral. Petrogr. Mitt.* **78**, 243–255.

Zhang H. F., Sun M., Zhou X. H. and Ying J. F. (2005) Geochemical constraints on the origin of Mesozoic alkaline intrusive complexes from the North China Craton and tectonic implications. *Lithos* **81**, 297–317.

Zhang H. F., Sun M., Zhou X. H., Fan W. M. and Zheng J. P. (2003) Secular evolution of the lithosphere beneath the eastern North China Craton: evidence from Mesozoic basalts and high-Mg andesites. *Geochim. Cosmochim. Acta* **67**, 4373–4387.

Zhang H. F., Sun M., Zhou X. H., Fan W. M., Zhai M. G. and Yin J. F. (2002) Mesozoic lithosphere destruction beneath the North China Craton: evidence from major, trace element, and Sr–Nd–Pb isotope studies of Fangcheng basalts. *Contrib. Miner. Petrol.* **144**, 241–253.

Zhang Y., Ni H. and Chen Yan (2010) Diffusion data in silicate melts. In *Diffusion in Minerals and Melts* (eds. Y. Zhang and D. J. Cherniak). Mineralogical Society of America, Chantilly, pp. 311–408.

Zhang Y., Walker D. and Lesher C. E. (1989) Diffusive crystal dissolution. *Contrib. Mineral. Petrol.* **102**, 492–513.

Zhang Y. and Xu Z. (2003) Kinetics of convective crystal dissolution and melting, with applications to methane hydrate dissolution and dissociation in seawater. *Earth Planet. Sci. Lett.* **213**, 133–148.

Zhao G., Cawood P. A., Wilde S. A., Sun M. and Lu L. (2000) Metamorphism of basement rocks in the Central Zone of the North China Craton: implications for Paleoproterozoic tectonic evolution. *Precambrian Res.* **103**, 55–88.

Zhao G., Wilde S. A., Cawood P. A. and Sun M. (2001) Archean blocks and their boundaries in the North China Craton: lithological, geochemical, structural and P-T path constraints and tectonic evolution. *Precambrian Res.* **107**, 45–73.

Zheng J. P., O'Reilly S. Y., Griffin W. L., Lu F. X., Zhang M. and Pearson N. J. (2001) Relict refractory mantle beneath the eastern North China block: significance for lithosphere evolution. *Lithos* **57**, 43–66.

Zheng J. P., Griffin W. L., O'Reilly S. Y., Yu C. M., Zhang H. F., Pearson N. and Zhang M. (2007) Mechanism and timing of lithospheric modification and replacement beneath the eastern north China Craton: peridotitic xenoliths from the 100 Ma Fuxin basalts and a regional synthesis. *Geochim. Cosmochim. Acta* **71**, 5203–5225.

Zhou X. H., Sun M., Zhang G. H. and Chen S. H. (2002) Continental crust and lithospheric mantle interaction beneath North China: isotopic evidence from granulite xenoliths in Hannuoba, Sino-Korean craton. *Lithos* **62**, 111–124.

Zhu R. X., Yang J. H. and Wu F. Y. (2012) Timing of destruction of the North China Craton. *Lithos* **149**, 51–60.

Associate editor: Fang-Zhen Teng